The Ages of Passive Galaxies in a $z = 1.62$ Protocluster

By

Donald B. Lee-Brown

Submitted to the graduate degree program in the Department of Physics and Astronomy and the Graduate Faculty of the University of Kansas in partial fulfillment of the requirements for the degree of Master of Science

Dr. Gregory H. Rudnick, Chairperson

Committee members

Dr. Barbara J. Anthony-Twarog

Dr. Steven A. Hawley

Date defended: November 18, 2016

The Thesis Committee for Donald B. Lee-Brown certifies
that this is the approved version of the following thesis :

The Ages of Passive Galaxies in a $z = 1.62$ Protocluster

Dr. Gregory H. Rudnick, Chairperson

Date approved: November 22, 2016

Abstract

Understanding how galaxies stop forming stars is a principle pursuit of extragalactic astrophysics. Here, I present a study of the relation between galaxy stellar age and mass in the $z = 1.62$ protocluster IRC 0218. After separating star forming and quiescent galaxies on the basis of their UVJ colors, we find that at stellar masses $M_* \geq 10^{10.8} M_\odot$, the quiescent fraction in IRC 0218 is $f_Q = 1.0^{+0.00}_{-0.36}$, approximately $2-3\times$ higher than the field value. At lower masses, f_Q is consistent with the field. Using galaxy $D_n(4000)$ values as measures of stellar age, we find no relation between age and mass. This may indicate that the mass dependence of f_Q was imprinted early in IRC 0218's history. Alternatively, the lack of a relation may be due to mass redistribution through gasless merging. Ultimately, our results place constraints on the mechanism(s) responsible for quenching in dense environments at $z \geq 1.5$.

Acknowledgements

What started as a short-term side project clearly grew into something a bit bigger, and I am greatly indebted to Dr. Gregory Rudnick for his generosity in time, guidance, and patience. Additionally, many thanks are in order to Dr. Barbara Anthony-Twarog and Dr. Bruce Twarog, for allowing their overly-optimistic graduate student to see this project to completion as it grew in both scope and time comittment. Finally, despite her refusal to allow me to subsist entirely on a diet of hamburgers, I would undoubtedly still be floundering around amongst piles of data were it not for the extraordinary care and support of my wife, Hannah.

Contents

List of Figures

List of Tables

Chapter 1

Introduction

In the local Universe, galaxies populate two distinct regions in color-magnitude space. Red, massive galaxies with predominantly early-type morphologies and little or no ongoing star formation form a tight relation known as the *red sequence*, while the *blue cloud* consists of lower-mass, star forming galaxies with late-type morphologies (Kauffmann et al., 2003). This bimodality is unambiguously observed to redshifts $z > 2$ (e.g. Kriek et al. 2008; Williams et al. 2009; Whitaker et al. 2013), and massive quiescent galaxies have been detected as early as $z \sim 4$ (Straatman et al., 2014).

The properties of galaxies also depend on their environment. Numerous studies have found an inverse relation between star formation rate (SFR) density and galaxy overdensity, such that the SFR density in cluster cores is much lower than that of the field (e.g. Hashimoto et al. 1998; Lewis et al. 2002; Gómez et al. 2003; Hogg et al. 2004; Balogh et al. 2004; Patel et al. 2009). Additionally, by $z \sim 0$, the fraction of quiescent, lower-mass cluster galaxies relative to the field is significantly enhanced and approaches the value for the more massive central galaxies (Tal et al., 2014). These results indicate that in addition to the intrinsic mechanisms responsible for the field red sequence, environmentally-driven processes exist and may even play a dominant role in the quenching of lower-mass galaxies (e.g. Bassett et al. 2013; Delaye et al. 2014). A comprehensive understanding of the physical processes responsible for quiescence and their relative importances as a function of galaxy mass and environment is one of the primary objectives in extragalactic

astrophysics.

Attempts to observe dynamically young clusters, where massive ($M_* \geq 10^{10} M_\odot$) quiescent galaxies are building up the bulk of their stellar populations and actively shutting off star formation, have naturally pushed to higher redshifts. At $z \geq 1$, the cluster environment is strikingly different than that observed at lower redshifts, with many clusters showing evidence for high fractions of star forming galaxies (e.g. Tadaki et al. 2012; Brodwin et al. 2013), recent or ongoing merging (Rudnick et al., 2012; Lotz et al., 2013), and star forming early-type galaxies (Mei et al., 2015). Perhaps the most striking difference, however, is that the well-known $z \sim 0$ inverse relation between SFR density and galaxy overdensity appears to reverse between $z = 1$ and $z = 1.5$ (Tran et al. 2010; Tadaki et al. 2012; Brodwin et al. 2013; Alberts et al. 2014, though see Gobat et al. 2011; Quadri et al. 2012). This observed trend is generally interpreted as being indicative of decreasing environmental impact on star formation rate as redshift increases (e.g., Quadri et al., 2012; Brodwin et al., 2013; Fassbender et al., 2014; Nantais et al., 2016).

Still, even at $z \geq 1.5$, the environment likely still plays an important, though secondary, role in cluster red sequence assembly. In recent years a steadily increasing number of high-redshift ($z > 1.5$) clusters or protoclusters have been discovered and confirmed (e.g. Andreon et al. 2009; Papovich et al. 2010; Gobat et al. 2011; Santos et al. 2011; Stanford et al. 2012; Zeimann et al. 2012; Mei et al. 2015; Cooke et al. 2016). What studies have found is that while significant cluster-to-cluster scatter exists, $z \geq 1.5$ clusters still have elevated quiescent fractions relative to the field (Quadri et al. 2012; Newman et al. 2014; Cooke et al. 2016; Nantais et al. 2016, though see Lee et al. 2015). However, it is not yet clear what mechanisms drive the observed enhanced quiescent fractions.

To address this deficiency, we focus in this work on one high-redshift dense environment, the $z = 1.62$ protocluster XMM-LSS J02182-05102 (also known as IRC 0218 and hereafter referred to as such). The protocluster was identified as an overdensity in red *Spitzer*/IRAC colors coincident with weak *XMM* X-ray emission, and subsequently spectroscopically confirmed with IMACS (Papovich et al., 2010). It was simultaneously and independently discovered and confirmed through

similar methods by Tanaka et al. (2010). Various followup studies have built up a wealth of multi-band photometric and spectroscopic observations (see Chapter 2.1) making the protocluster an important object for the study of high-redshift dense environments.

IRC 0218's mass is estimated to be relatively low, around $M \sim 4-7 \times 10^{13} M_{\odot}$ (Papovich et al., 2010; Finoguenov et al., 2010; Pierre et al., 2012; Tran et al., 2015), formally identifying it as a group/protocluster and making it a likely progenitor of a Virgo-mass cluster ($M \sim 10^{14} M_{\odot}$) in the local Universe (Hatch et al., 2016). The weakness of its intracluster X-ray emission as observed by *Chandra* indicates that it is not yet virialized (Pierre et al., 2012), with recent work supporting this and finding that the protocluster actually consists of several distinct subgroups in the process of assembly (Hatch et al., 2016).

The protocluster's unevolved state and low velocity dispersion suggest a much higher merger rate than in more mature cluster environments (Papovich et al., 2010; Pierre et al., 2012; Rudnick et al., 2012; Hatch et al., 2016). Indeed, morphological studies of the red sequence population have found a lack of compact quiescent galaxies, attributed to a previous and/or currently increased merger rate in the protocluster relative to the field (Papovich et al., 2012). This explanation is supported by the direct-imaging study of Lotz et al. (2013), which found that the merger rate for the massive galaxies ($M_* \geq 10^{10} M_{\odot}$) is a factor of 3-10 higher than that in the field, with the bulk of the extra merging due to dry minor merging.

Since IRC 0218 has a relatively well-developed red sequence, is still in the process of assembly, and shows evidence for elevated merger activity, it is an excellent target for investigating the buildup of the high-redshift red sequence in dense environments. In this work, we examine the relation between galaxy mass and $D_n(4000)$ (which we use as a proxy for stellar age) in order to constrain the possible explanations for the buildup of the red sequence in dense environments. For example, if mass is the primary driver of quenching at high redshifts and cluster galaxies merely assembled earlier than in the field, then there should be a clear relation between age and stellar mass. On the other hand, if, e.g., mergers have played a significant role in the buildup of the cluster's red sequence, we expect little to no relation between mass and age on the red sequence.

The outline of this work is as follows. Our data is described in Chapter 2.1. In Chapter 2.2 we explain how we selected our cluster and field samples, measured stellar masses and the $D_n(4000)$ spectroscopic index (Bruzual A., 1983; Balogh et al., 1999), and estimated sample completeness. In Chapter 3.1 we discuss the quiescent fraction of galaxies in the cluster and field samples, and use the measurements of $D_n(4000)$ to constrain age differences between quiescent and star forming cluster galaxies. Finally, we discuss our results in Chapter 3.2, compare them with the results of other high-redshift galaxy cluster studies, and conclude in Chapter 4. Throughout, we use a ΛCDM cosmology with $\Omega_m = 0.3$,$\Omega_\Lambda = 0.7$, and $H_0 = 70$ km s^{-1} Mpc^{-1}, and a Chabrier IMF (Chabrier, 2003). Magnitudes given are on the AB system with zeropoint $M_{AB} = 25$.

Chapter 2

Data

2.1 Data

IRC 0218 is in the UKIDSS Ultra-Deep Survey field (UDS; Lawrence et al. 2007) and was partially imaged with the WFC3 F125W (J_{125}) and F160W (H_{160}) filters as part of the CANDELS survey (Grogin et al. 2011; Koekemoer et al. 2011). Full CANDELS-depth photometric coverage of the cluster in F125W and F160W, as well as 10 orbits of G102 grism spectroscopy, were obtained under a followup program (PI Papovich: GO 12590). Additionally, we use WFC3 F140W filter and G141 grism coverage of the cluster collected under the 3D-HST survey (Brammer et al., 2012; Momcheva et al., 2016). The photometry used for this study is contained in the v4.1.5 3D-HST release, and was self-consistently reduced as described in Skelton et al. (2014), and both G102 and G141 data were reduced according to the procedure described in Momcheva et al. (2016).

The G102 grism provides low-resolution ($R \sim 210$) spectroscopy of wavelengths $800 \leq \lambda \leq 1150$ nm, while the G141 grism covers $1075 \leq \lambda \leq 1700$ nm with $R \sim 130$. Thus, the grism observations cover the rest-frame 4000 Å (Balmer) break, the 3727 Å [OII] region, and the 4959 Å and 5007 Å [OIII] features at the redshift of the protocluster. The range of spectroscopic coverage provided by the two grisms, as well as the extensive photometric data, together enable precise redshift determinations through SED fitting. Several example grism spectra and their accompanying SED fits are given in Figure 2.1.

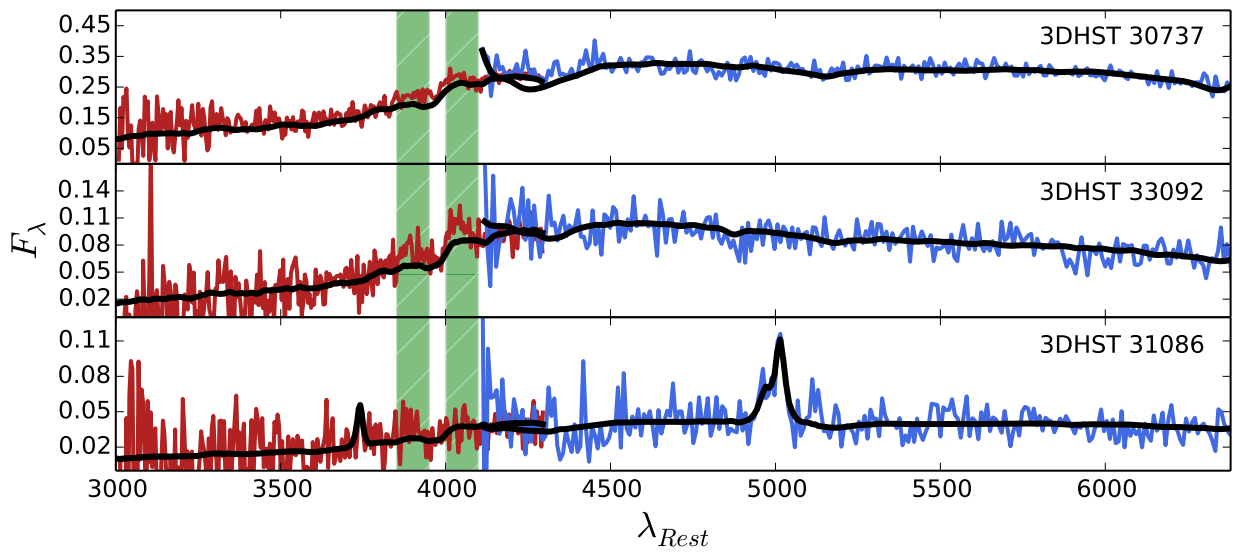

Figure 2.1: Rest-frame G102 (red) and G141 (blue) grism spectra of three galaxies in IRC 0218, plotted from $\sim$ 3000-6850 Å. The colored lines are measured fluxes, and the black lines are best-fit SED models. The two grism spectra for each galaxy were fit independently, resulting in some model discontinuity where the grism wavelength ranges overlap, $\sim$ 4200 Å. The vertical green bars denote the upper and lower $D_n(4000)$ indices (see Chapter 3.1).

As a final note, some of the galaxies in IRC 0218 have redshifts derived from higher resolution ground-based spectroscopy (Subaru/MOIRCS: Tanaka et al. 2010, Magellan/IMACS: Papovich et al. 2010, KECK/MOSFIRE+LRIS: Tran et al. 2015). The cases where these redshifts were adopted are indicated in Table A.1. In general, preference was given to these redshifts except in three cases where the grism-based redshifts were indisputably superior. The procedure by which the grism redshifts were derived is detailed in Chapter 2.2.2.

2.2 Sample Selection and Completeness

2.2.1 The Field and Protocluster Grism Samples

We select our spectroscopic field and protocluster samples from the galaxies with G102 coverage of the rest-frame 4000 Å break, which limits our samples to galaxies in the redshift range $1.27 \leq z \leq 1.77$. Additionally, the spatial extent of the spectroscopic samples are limited to the single 3D-HST field UDS-18, the only field for which we have the requisite G102 coverage. Comparison of

the SED fit-derived grism+photometric redshifts with those obtained by higher resolution ground-based spectroscopy indicates an average deviation of $\overline{\Delta z} = 0.01$ at the protocluster redshift, so we construct the cluster sample using all 25 galaxies with redshifts $z = 1.62 \pm 0.02$ in the field. For the field sample, we use all 38 galaxies in the field with redshifts $1.27 \leq z \leq 1.58$, $1.66 \leq z \leq 1.77$.

2.2.2 Measurement of Stellar Masses and $D_n(4000)$

Stellar masses for the protocluster and field galaxies were estimated through template fits to the rest-frame photometry, using the fitting code FAST (Kriek et al., 2009). For the template fits, we adopted the maximally likely redshifts from the redshift probability distributions derived from available G141, G102, and photometric data. As a galaxy's redshift probability distribution is, in general, non-Gaussian, upper and lower 68% redshift confidence intervals were estimated through resampling. The protocluster sample contains 15 galaxies with precision redshifts measured from high-resolution spectroscopy, and for these galaxies we fix their redshifts to the spectroscopic values. Bruzual & Charlot (2003) stellar population models were used to generate templates with metallicity fixed at $Z = 0.02$, ages A in the range $10^{7.6} \leq A(yr^{-1}) \leq 10^{10.1}$, and exponentially declining star formation histories with τ in the range $10^7 \leq \tau(yr^{-1}) \leq 10^{10}$ yr. The dust law of Calzetti et al. (2000) was adopted for the template fitting, though we note that galaxy mass is relatively insensitive to the specific choice of dust law.

The rest-frame 4000 Å break is due to line blanketing - primarily Ca and Fe lines - of the stellar continuum emission from lower-mass (F, G, and K spectral type) dwarfs and giants. Young stellar populations will have weak 4000 Å breaks due to the luminosity contribution from high-mass stars, and old populations with prominent absorption lines will have the strongest 4000 Å breaks. Thus, the $D(4000)$ spectroscopic index (Bruzual A., 1983), defined to be the ratio of flux above the 4000 Å break to the flux below it, provides a straightforward estimate of a galaxy's luminosity-weighted age (see, e.g, Rudnick et al. 2000; Kauffmann et al. 2003). In this work, we adopt the wavelength definitions of Balogh et al. (1999), i.e., the index is defined to be the ratio of mean rest-frame flux in the region $4000 \leq \lambda \leq 4100$ to the flux in the region $3850 \leq \lambda \leq 3950$, and we denote this as

$D_n(4000)$. The principle advantage of $D_n(4000)$ over the original index definition of Bruzual A. (1983) is its insensitivity to reddening effects.

The method used to estimate the uncertainties in $D_n(4000)$ is as follows. First, one-dimensional optimally-weighted spectra were extracted from the 2-D G102 grism spectra following the method of Horne (1986). Next, a redshift was randomly drawn from the per-galaxy redshift probability grid derived from jointly fitting the G102, G141, and photometric data. For the joint-fit redshifts, typical redshift probability grid step sizes are $\Delta z \leq 10^{-3}$; we nonetheless linearly interpolated onto a 10x denser grid before the random draw. If a galaxy had an adopted ground-based spectroscopic redshift, this redshift was selected instead and fixed. Finally, under the assumption of normally distributed flux uncertainties, the flux in each wavelength bin was randomly drawn, and appropriately redshifted $D_n(4000)$ calculated. Linear interpolation was used to estimate the flux in partial wavelength bins at the index boundaries. After several thousand iterations of this process for each galaxy, upper and lower 68% confidence intervals were calculated for each measured $D_n(4000)$.

2.2.3 Completeness

We estimated the spectroscopic completeness of our sample by comparing the G102 sample with the much deeper photometric catalog in the spatial region of the protocluster. We find that 90% of the photometric sources with $J_{AB} \leq 22.6$ have extracted grism spectra (Figure 2.2).This limiting magnitude was then used to obtain an empirical estimate of the spectroscopic mass completeness, following the procedure of Marchesini et al. 2009. To do this, we selected *photometric* sources with $22.0 \leq J_{AB} \leq 23.0$ and redshifts $1.40 \leq z \leq 1.75$, and scaled their J_{AB} luminosities to the $J_{AB} \leq 22.6$ spectroscopic limit, holding galaxy mass-to-light ratio (M/L) constant. Under the assumption that the distribution of galaxy M/L is unchanged over the magnitude and redshift ranges we used, the luminosity scaling process creates a simulated, relatively complete population at the spectroscopic limit. The high-mass end of the simulated population then gives an estimate of the mass completeness. We find our 95% grism mass-completeness limit to be $10^{10.2} M_{\odot}$. In the protocluster, $14/25$ extracted grism sources are above the mass completeness limit, and in the field

12/38 sources are above the cutoff.

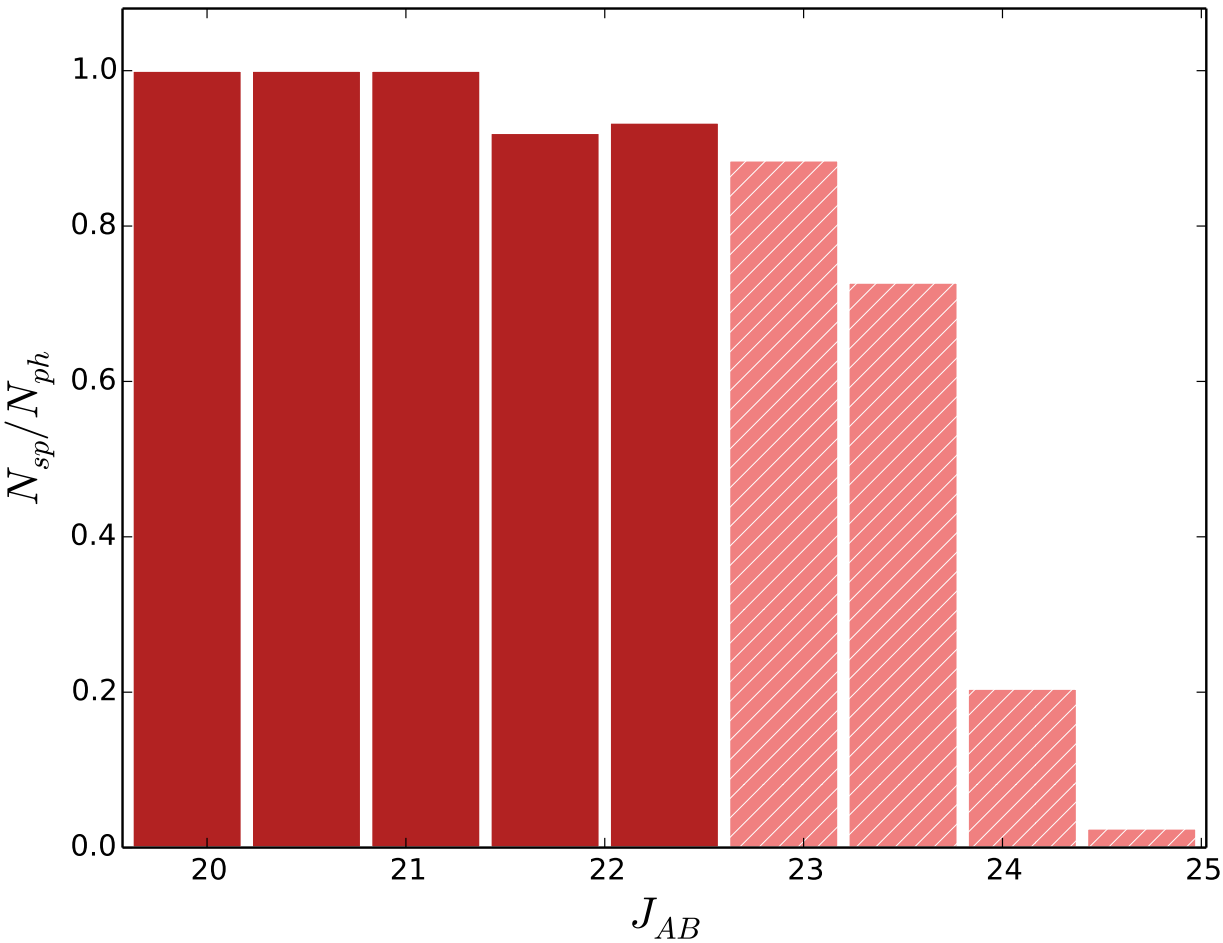

Figure 2.2: G102 completeness, given as the ratio of spectroscopic to photometric detections, as a function of 3D-HST J_{AB} magnitude. Solid bars indicate galaxies above our 90% spectroscopic completeness limit, which occurs at $J_{AB} = 22.6$.

Chapter 3

Results and Discussion

3.1 Results

3.1.1 The Quiescent Fraction in IRC 0218 and the Field

The protocluster and field samples were separated into quiescent and star forming populations according to their positions in the $(U-V)$,$(V-J)$ plane, following the work by Wuyts et al. (2007) and Williams et al. (2009). Separating galaxies in the UVJ plane allows for a dinstinction between quiescent galaxies and dust-obscured, star forming galaxies that might appear quiescent based on their $(U-V)$ colors alone. The results of this selection process are given in Figure 3.1 and Figure 3.2.

We find that above our mass completeness limit, $8/14$ protocluster and $2/12$ field galaxies meet our adopted requirements for quiescence. Defining the quiescent fraction as $f_Q = n_Q/(n_{SF}+n_Q)$, where n_Q and n_{SF} are the numbers of quiescent and star forming galaxies, respectively, we find that $f_Q = 0.57^{+0.15}_{-0.16}$ in the protocluster, and $f_Q = 0.17^{+0.17}_{-0.11}$ in the field. The upper and lower uncertainties given are the 68% binomial confidence intervals calculated according to Gehrels (1986).

As our definition of quiescence only uses UVJ information and our stellar mass values are derived from photometry, we can extend the field sample to include all galaxies with masses $M_* \geq$

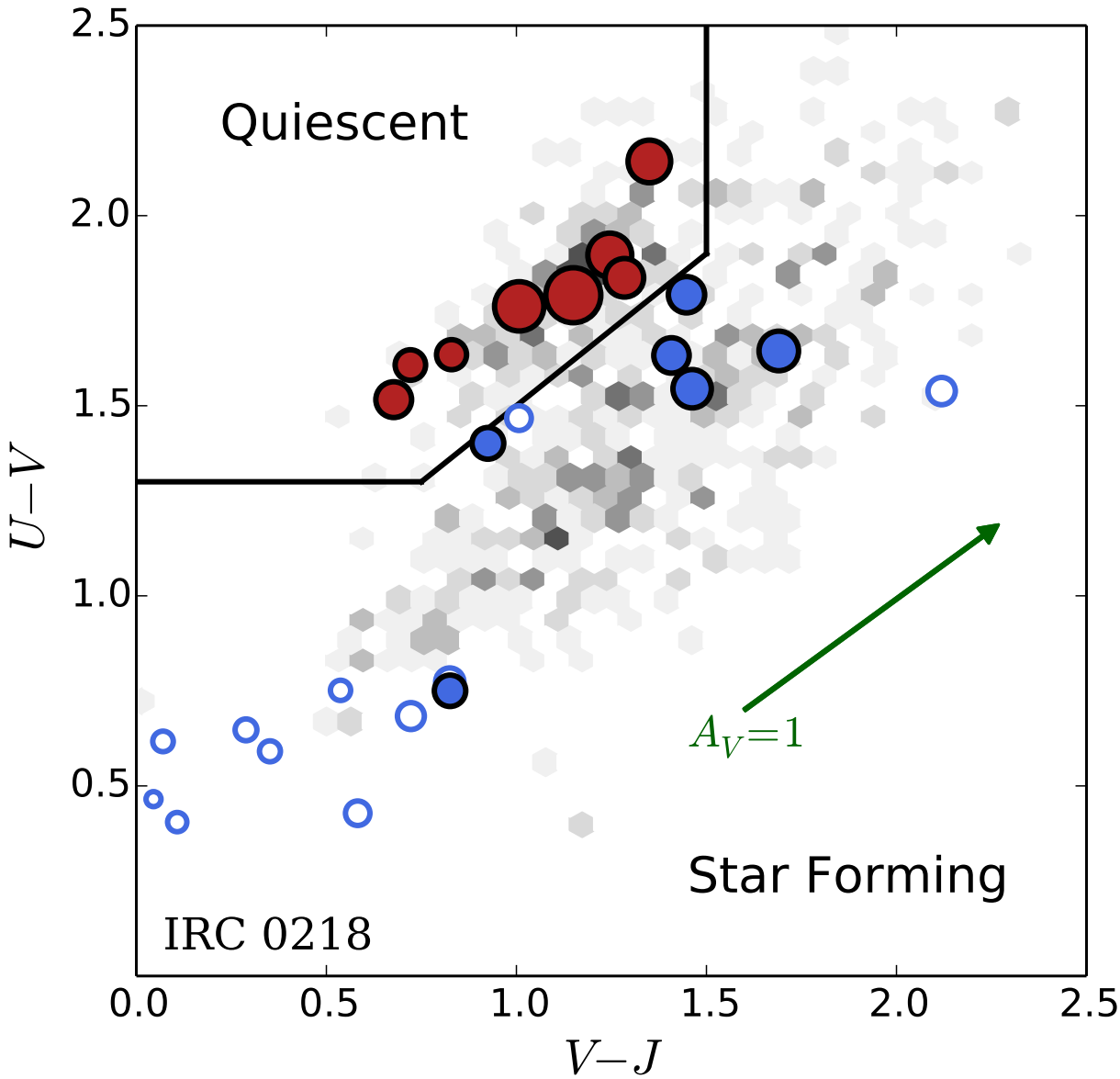

Figure 3.1: $(U-V)$, $(V-J)$ color-color diagram for the protocluster sample. Points in the upper left bounded region of each plot are classified as quiescent, while points outside the region are classified as star forming. Point size indicates mass scaled relative to the most massive quiescent protocluster galaxy, $M_* = 10^{11.48} M_\odot$. Open points represent galaxies below the adopted mass completeness threshold of $M_* = 10^{10.2} M_\odot$. The grayscale region shows the colors of the full 3D-HST G141 grism sample above the mass completeness threshold in the redshift range $1 \leq z \leq 2$. The arrow indicates the change in $(U-V)$ and $(V-J)$ expected for a one magnitude increase in reddening in V_{AB}, following the Calzetti et al. (2000) extinction law.

$10^{10.2} M_\odot$ and redshifts $1.40 \leq z \leq 1.54$, $1.70 \leq z \leq 1.90$, in order to avoid the larger uncertainties due to the small sample size of the G141+G102 derived field sample. The extended field sample

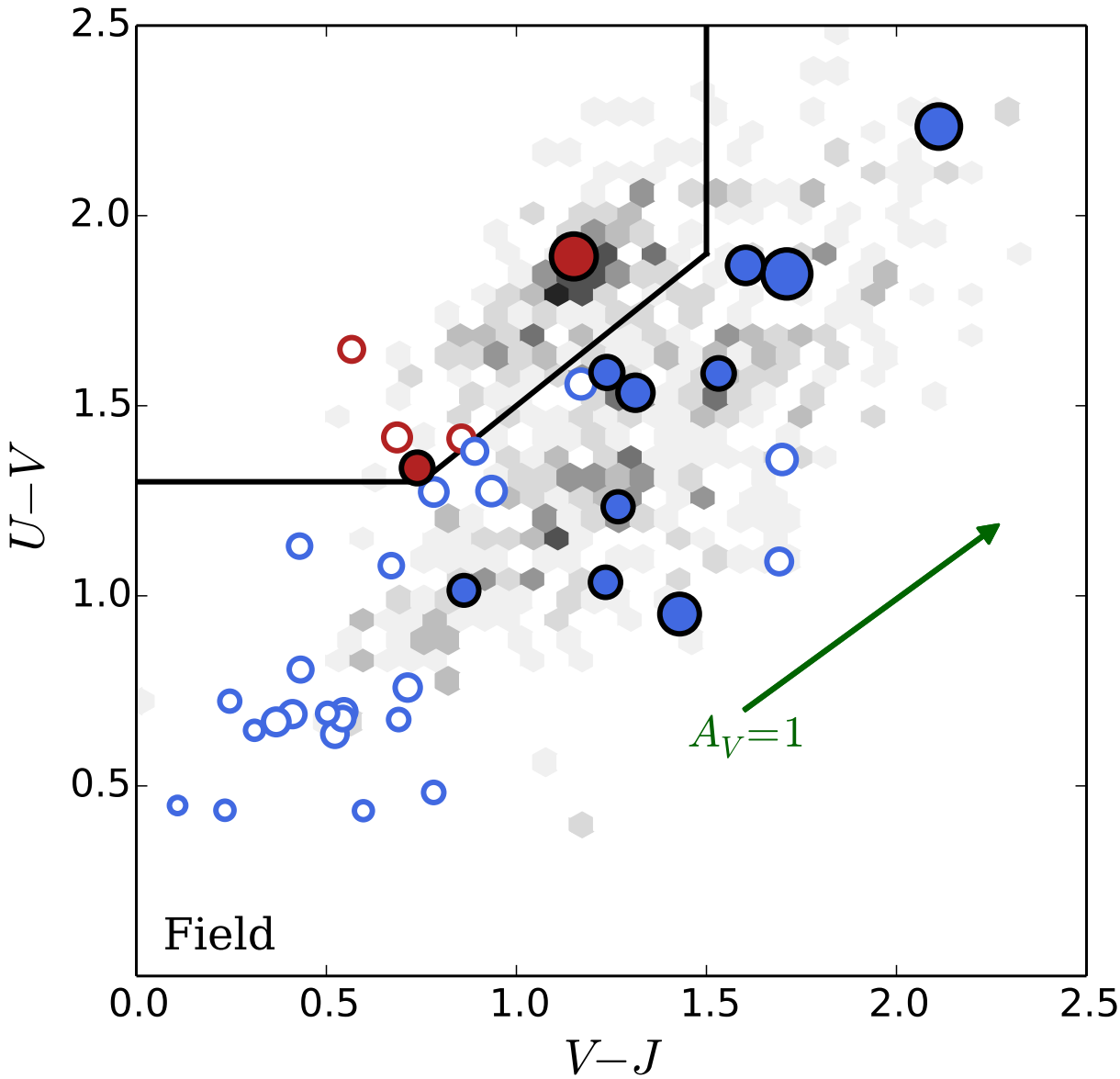

Figure 3.2: $(U-V)$, $(V-J)$ color-color diagram for the field sample. Format is identical to Figure 3.1.

has 248 galaxies with mass $M_* \geq 10^{10.2} M_\odot$: 67 quiescent and 177 star forming, according to their UVJ plane positions. From this sample we obtain $f_Q = 0.27^{+0.03}_{-0.02}$, consistent with the G141+G102 sample, though considerably more precise. Thus, we conclude that considering all galaxies with $M_* \geq 10^{10.2} M_\odot$, the protocluster is approximately $2-3\times$ as quenched as the field.

We also examined f_Q as a function of stellar mass for the field and protocluster. To do this, we binned the protocluster and field samples by mass, and calculated f_Q in each bin. For the

Table 3.1. Mass and f_Q

$log(M/M_\odot)$	N_{Q+SF}	N_Q	f_Q
	IRC 0218		
11.175	4	4	$1.00^{0.00}_{0.36}$
10.525	4	6	$0.40^{0.20}_{0.18}$
	Field		
11.3	8	3	$0.27^{0.20}_{0.14}$
11.1	12	6	$0.33^{0.15}_{0.12}$
10.9	30	17	$0.36^{0.08}_{0.08}$
10.7	40	13	$0.25^{0.07}_{0.06}$
10.5	38	15	$0.28^{0.07}_{0.07}$
10.3	49	13	$0.21^{0.06}_{0.05}$

Note. — Only the mass-complete protocluster sample considered here. Masses correspond to bin centers; bin widths are $\Delta log(M/M_\odot) = 0.65$ for the cluster and $\Delta log(M/M_\odot) = 0.40$ for the field.

protocluster sample, we constructed two mass bins, where the boundary between the bins was taken to be the midpoint of the range in mass spanned by the most massive protocluster galaxy and the mass completeness limit. For the field, galaxies were separated into 6 equal-width mass bins spanning $10^{10.2} \leq M_* \leq 10^{11.4}$. The results of this process are given in Table 3.1.

We find that in the mass range $10^{10.2} M_\odot \leq M_* \leq 10^{10.8} M_\odot$, f_Q in the protocluster is consistent with value in the field. Within the protocluster, the difference between low and high mass galaxy bins is marginally significant; in the high mass bin, $f_Q = 1.0^{+0.00}_{-0.36}$, while in the low mass bin, $f_Q = 0.4^{+0.20}_{-0.18}$. However, over the same mass ranges, f_Q in the field is $f_Q = 0.34^{+0.06}_{-0.05}$ and $f_Q = 0.24^{+0.04}_{-0.03}$, respectively. Thus, at high masses, the protocluster is significantly more quenched than the field, while at low masses the protocluster and field f_Q values are consistent with one another.

Moderate changes to the UVJ criteria used to select quiescent galaxies, e.g., reclassifying the three star forming galaxies near the Whitaker et al. (2012) quiescent selection box (see Fig-

ure 3.1), would slightly weaken our mass trend in f_Q. Reclassifying those three points results in $f_Q = 0.60^{+0.18}_{-0.20}$ for the $M_* \leq 10^{10.8} M_\odot$ bin. On the other hand, the high f_Q in the $M_* \leq 10^{10.8} M_\odot$ bin is robust; the galaxies in this mass range are well-separated from the UVJ selection boundary. Additionally, we note that slight changes to our mass completeness limit would leave our conclusion of an enhanced quenched fraction at high stellar masses unchanged.

3.1.2 $D_n(4000)$ and Stellar Mass

We now turn our attention to $D_n(4000)$ and its ability to constrain relative age differences between galaxies in IRC 0218. In Figure 3.3 and Figure 3.4 we show $D_n(4000)$ as a function of stellar mass for the protocluster and field G102+G141 samples, respectively, along with $D_n(4000)$ predicted by Bruzual & Charlot (2003) models with exponentially declining star formation histories and formation redshifts $2.0 \leq z_f \leq 4.0$.

The lack of spectroscopic redshifts and weak 4000 Å breaks lead to relatively uncertain $D_n(4000)$ measurements for star forming field galaxies. This, combined with the lack of quiescent field galaxies, precludes strong conclusions based on the field sample. We simply note that as expected, the quiescent field galaxies are consistent with having stopped their star formation a few Gyr prior to the epoch of observation, while the star forming galaxies are generally consistent with ongoing star formation.

Redshifts for protocluster galaxies are, on average, more precise due to the availability of ground-based spectroscopic redshifts, and the well-populated red sequence allows for comparison between star forming and quiescent galaxies. Figure 3.5 shows the results of a weighted linear regression fit to $D_n(4000)$ as a function of mass for the protocluster quiescent galaxies above our completeness limit. For the fit, galaxies were weighted by the inverse squared average of their respective upper and lower 68% confidence limits on $D_n(4000)$. Confidence intervals on the fit were estimated by bootstrapping. We find no significant evidence for a relation between $D_n(4000)$ and stellar mass for quiescent galaxies above our stellar mass limit.

The weighted mean $D_n(4000)$ values for the quiescent and star forming galaxies in IRC 0218

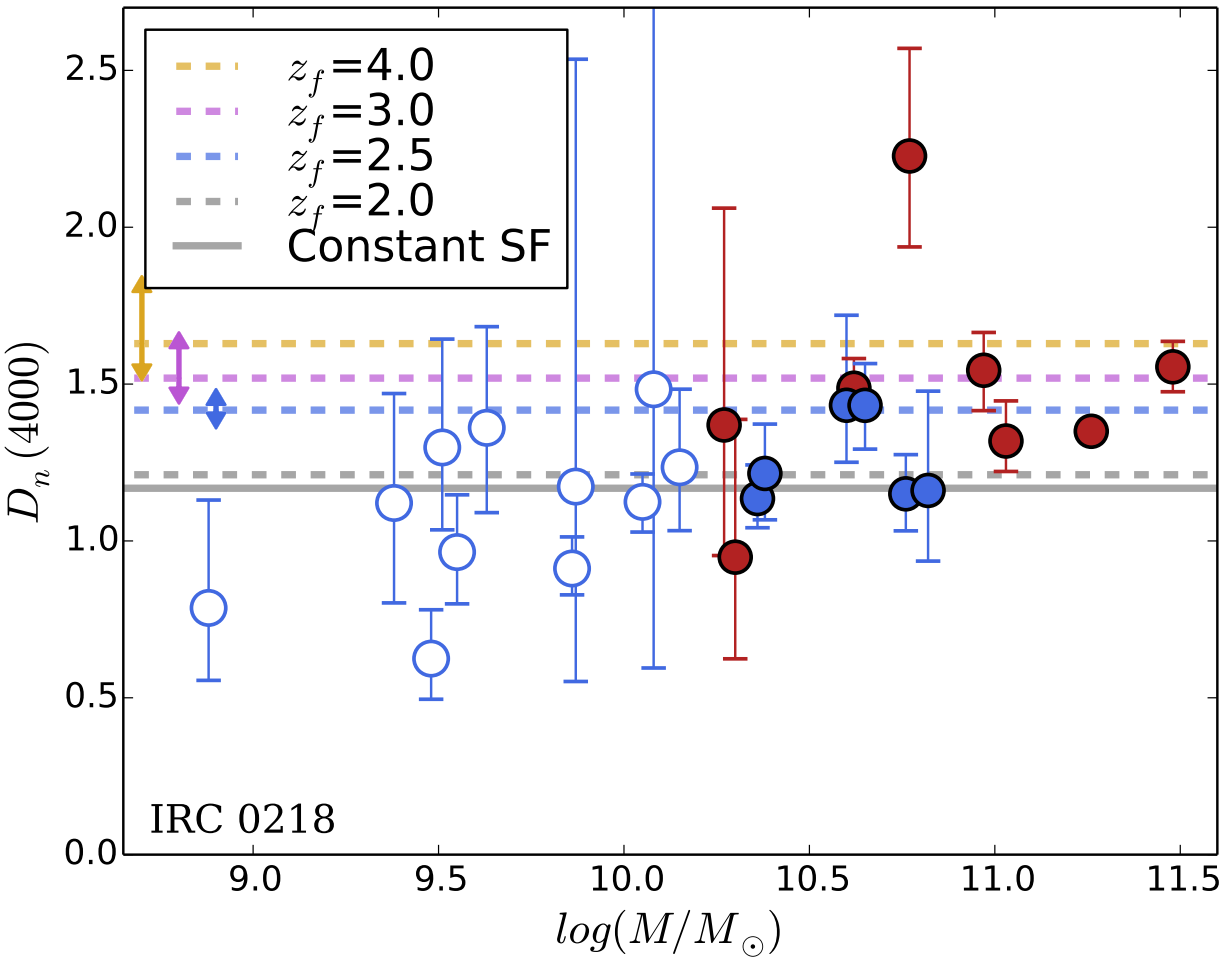

Figure 3.3: $D_n(4000)$ plotted against stellar mass for the protocluster G102 grism sample. Red and blue points represent quiescent and star forming galaxies, respectively, as determined by galaxy UVJ. Filled (open) points show galaxies above (below) the adopted mass completeness threshold. Error bars show the 68% $D_n(4000)$ confidence intervals, determined by resampling from the joint-fit G102 + G141 + photometry redshift probability distribution and flux uncertanties for each galaxy. For galaxies with high resolution spectroscopic redshifts, the error bars incorporate only flux uncertainties. Galaxies with large error bars generally have uncertain redshifts and/or low SN. The dashed horizontal lines show the $D_n(4000)$ predicted by Bruzual & Charlot (2003) galaxy spectral evolution models with $Z = 0.02$ and exponentially declining star formation histories ($\tau = 300$ Myr), for a variety of formation redshifts. The solid horizontal line indicates the $D_n(4000)$ expected for a model with constant star formation. Arrows attached to the exponential SFH model lines indicate the change in $D_n(4000)$ produced by changing galaxy metallicity to $Z = 0.05$ (upward arrows) or $Z = 0.004$ (downward arrows); the lines for $z_f = 2.0$ and constant star formation are virtually unchanged under these changes.

are $\mu_Q = 1.48 \pm 0.09$ and $\mu_{SF} = 1.27 \pm 0.15$, respectively. Under our adopted $\tau = 300$ Myr exponential SFH, we find that the quiescent galaxies in IRC 0218 are consistent with star formation

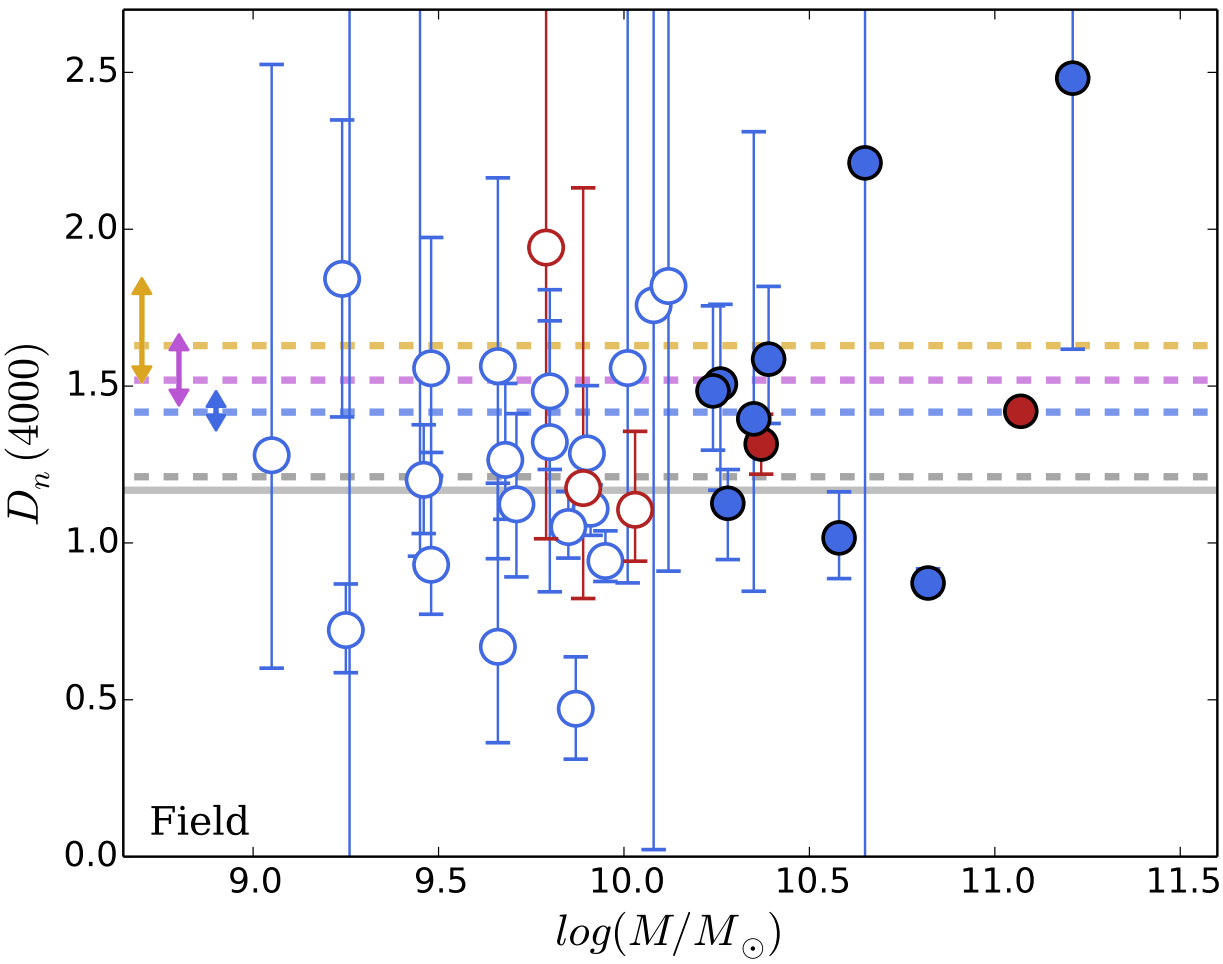

Figure 3.4: $D_n(4000)$ plotted against stellar mass for the field G102 grism sample. Format is identical to Figure 3.3. Two star-forming field galaxies from Table A.2 have extremely uncertain $D_n(4000)$ and are omitted from the figure

starting in the redshift range $2.3 \leq z_f \leq 3$. This formation epoch is consistent with the estimate by Papovich et al. (2010) on the basis of $(U-B)$ colors, and is similar to the formation redshifts estimated for several high-redshift clusters (e.g. Mei et al. 2009; Hilton et al. 2009). The star forming sample is consistent with ongoing or very recently truncated star formation.

These results are robust against moderate changes to the underlying UVJ quiescent/star forming classifications. Under the reclassification of the three galaxies discussed in Chapter 3.1.1, the significance of the difference between star forming and quiescent galaxies in IRC 0218 would be somewhat strengthened: $\mu_Q = 1.47 \pm 0.09$ and $\mu_{SF} = 1.14 \pm 0.03$. Under such a reclassification, there is still no relation between $D_n(4000)$ and galaxy mass. Additionally, as before, moderate

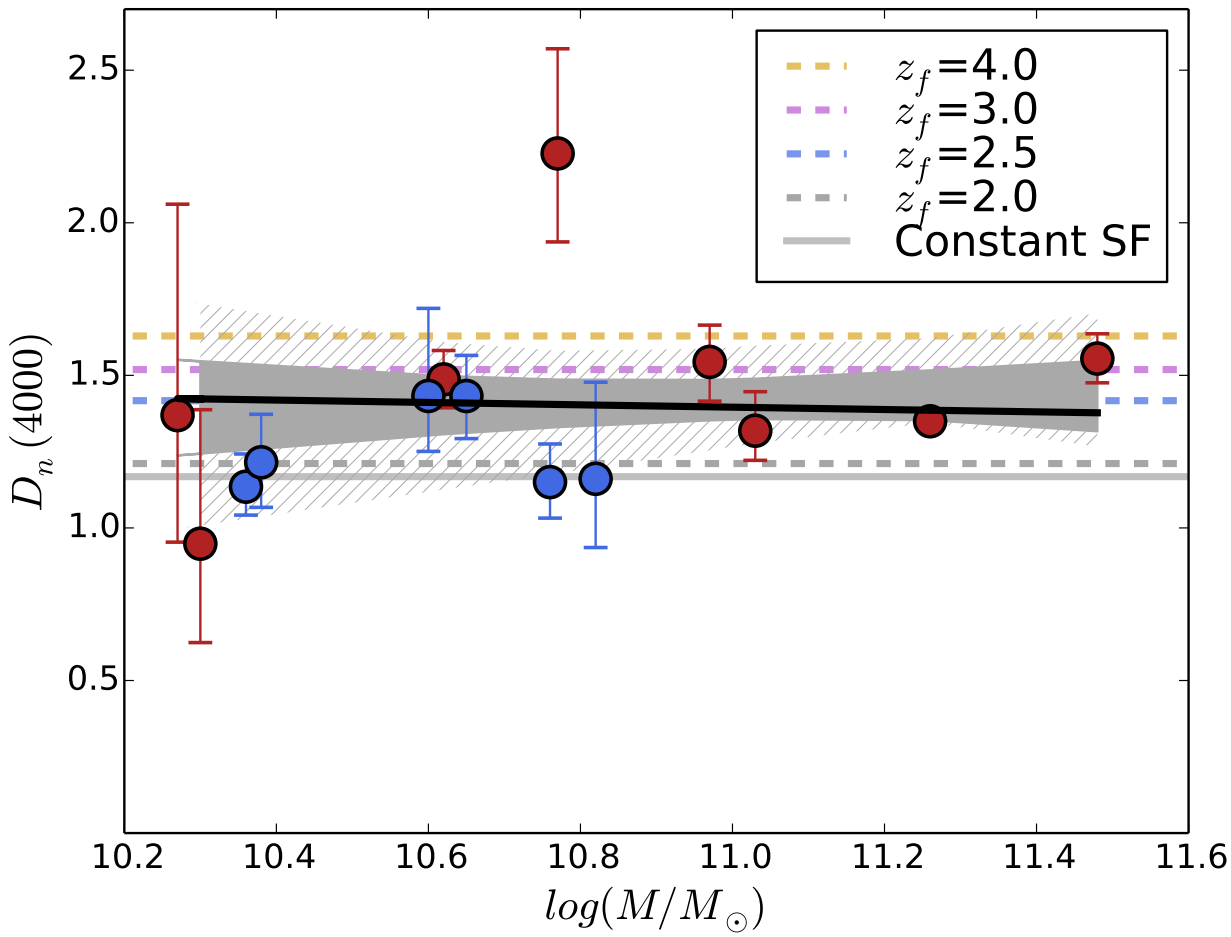

Figure 3.5: Weighted linear regression fit to $D_n(4000)$ as a function of mass for the quiescent protocluster galaxies. Only quiescent (red points) galaxies above the mass completeness limit were considered, with weights given by the inverse squared mean 68% confidence range in $D_n(4000)$. The solid (hatched) shaded region around the fit shows the upper and lower 68% (95%) confidence interval on the fit, as determined by bootstrapping. The dashed horizontal lines are the same as in Figure 3.3

changes to our mass completeness limit do not impact our results. Finally, we note that measurements of $D_n(4000)$ from simulated spectra degraded to the G102 grism resolution show no systematic offsets relative to measurements at higher resolutions (Henke, 2015).

3.2 Discussion

3.2.1 The Quiescent Fraction in IRC 0218

In IRC 0218, the quiescent fraction at $M_* \geq 10^{10.8} M_\odot$ is 2-3$\times$ higher than in the field. This elevated quiescent fraction is similar to that seen in the results from clusters at similar mass and redshift (Newman et al., 2014; Cooke et al., 2016), as seen in Figure 3.6. At masses below $M_* = 10^{10.8} M_\odot$, we find that the quiescent fraction in IRC 0218 is consistent with the field value, though our uncertainties mean we cannot rule out moderate (2$\times$) enhancements of f_Q as seen in Newman et al. (2014); Cooke et al. (2016).

Comparing our quiescent fraction results with those of other high redshift studies, as well as the GEEC2 and GCLASS results at $z \sim 1$ (Balogh et al., 2016), we find no evidence that the quiescent fraction at high stellar masses ($M_* \geq 10^{10.8} M_\odot$) evolves as a function of redshift over 1 $\leq z \leq 1.8$, as seen in Figure 3.7. The high quiescent fractions observed in dense environments at $z = 1$ and high stellar masses were already in place by $z = 1.5 - 1.8$, and possibly much higher given our $D_n(4000)$ results. The apparent lack of evolution in f_q stands in stark contrast with that observed in high mass galaxies in the field (see Figure 3.7), where the quiescent fraction changes dramatically between $z \sim 1$ and $z \sim 1.6$, indicating ongoing quenching activity in the field over this redshift range.

Drawing conclusions at lower halo masses is difficult, due to the uncertain masses of the high redshift clusters and small number statistics, but IRC 0218 is likely a progenitor of a typical $M_* = 10^{14} - 10^{14.5} M_\odot$ cluster at $z = 1$ (Rudnick et al., 2012), i.e., its likely descendent would be a GCLASS cluster, rather than a GEEC2 group. If this is so, then the lower stellar mass end would appear to evolve in its quiescent fraction over $1 \leq z \leq 1.8$, increasing by a factor of 1.5-3 for galaxies of mass $10^{10.2} M_\odot \leq M_* \leq 10^{10.8} M_\odot$. The JKCS 041 sample does not extend to low enough masses to test this conclusion, but the $z = 1.5$ Cooke et al. (2016) cluster is consistent with our inference from IRC 0218.

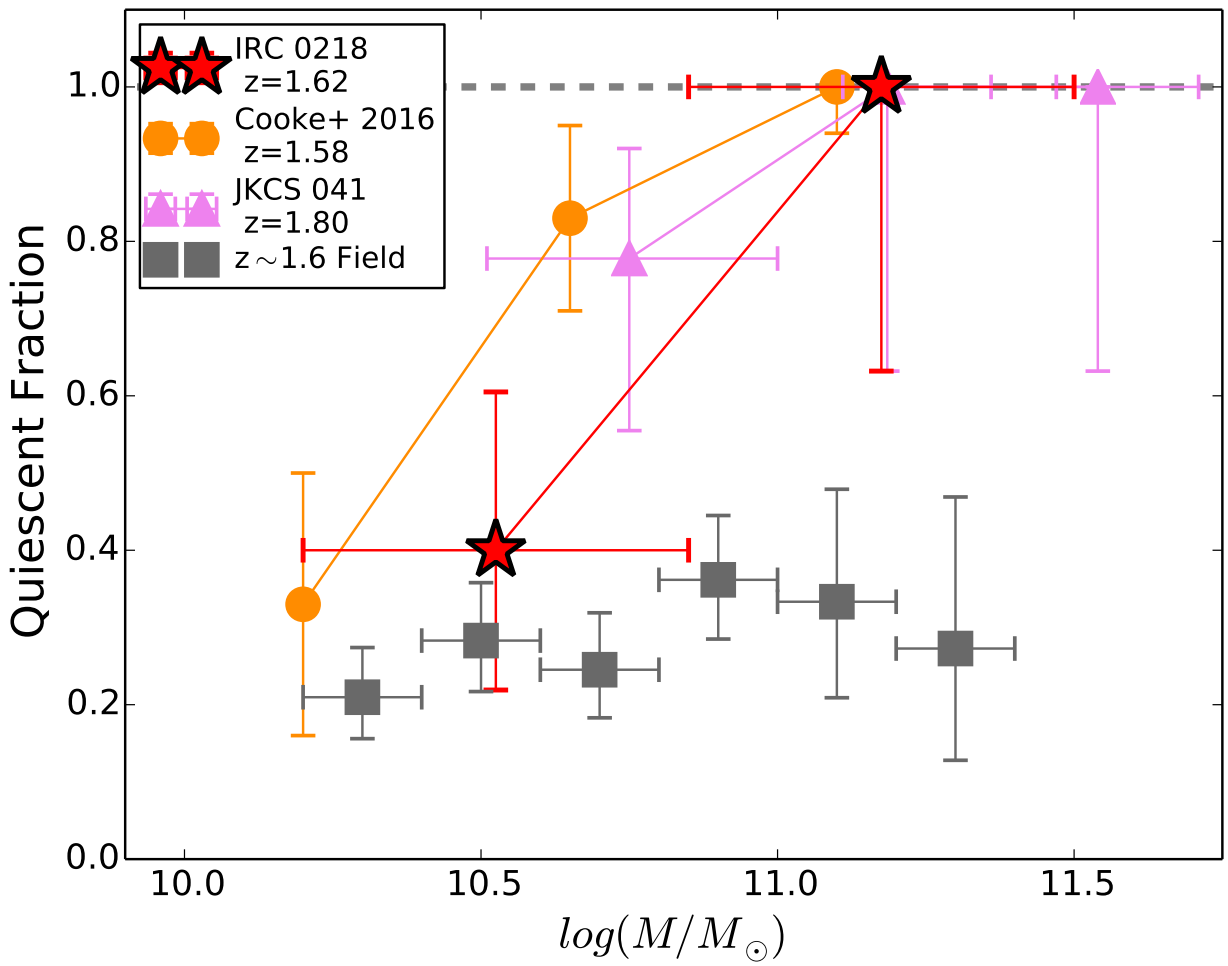

Figure 3.6: The quiescent fraction of galaxies as a function of stellar mass from this work (red stars), the Newman et al. (2014) study of the $z = 1.80$ cluster JKCS 041 (pink triangles), and the work by Cooke et al. (2016) on a $z = 1.58$ cluster near the radio galaxy 7C 1753+6311 (orange circles). The field sample (gray squares) is composed of all galaxies in the full 3D-HST G141 grism sample with redshifts $1.4 \leq z \leq 1.54$, $1.7 \leq z \leq 1.9$. Horizontal error bars span mass bin widths, and vertical error bars are from binomial counting statistics.

3.2.2 $D_n(4000)$ and Stellar Mass

We find no clear relation between $D_n(4000)$ and galaxy mass for the red sequence population in IRC 0218. This may indicate that the observed relation between quiescent fraction and stellar mass was in place very early in the protocluster's life, $z_f \sim 2.3 - 3.0$. That is, the high-mass galaxies observed to be quiescent at $z = 1.62$ moved to the red sequence at roughly the same epoch after relatively rapid quenching, creating the shape of the f_q-stellar mass relation observed in Figure 3.6.

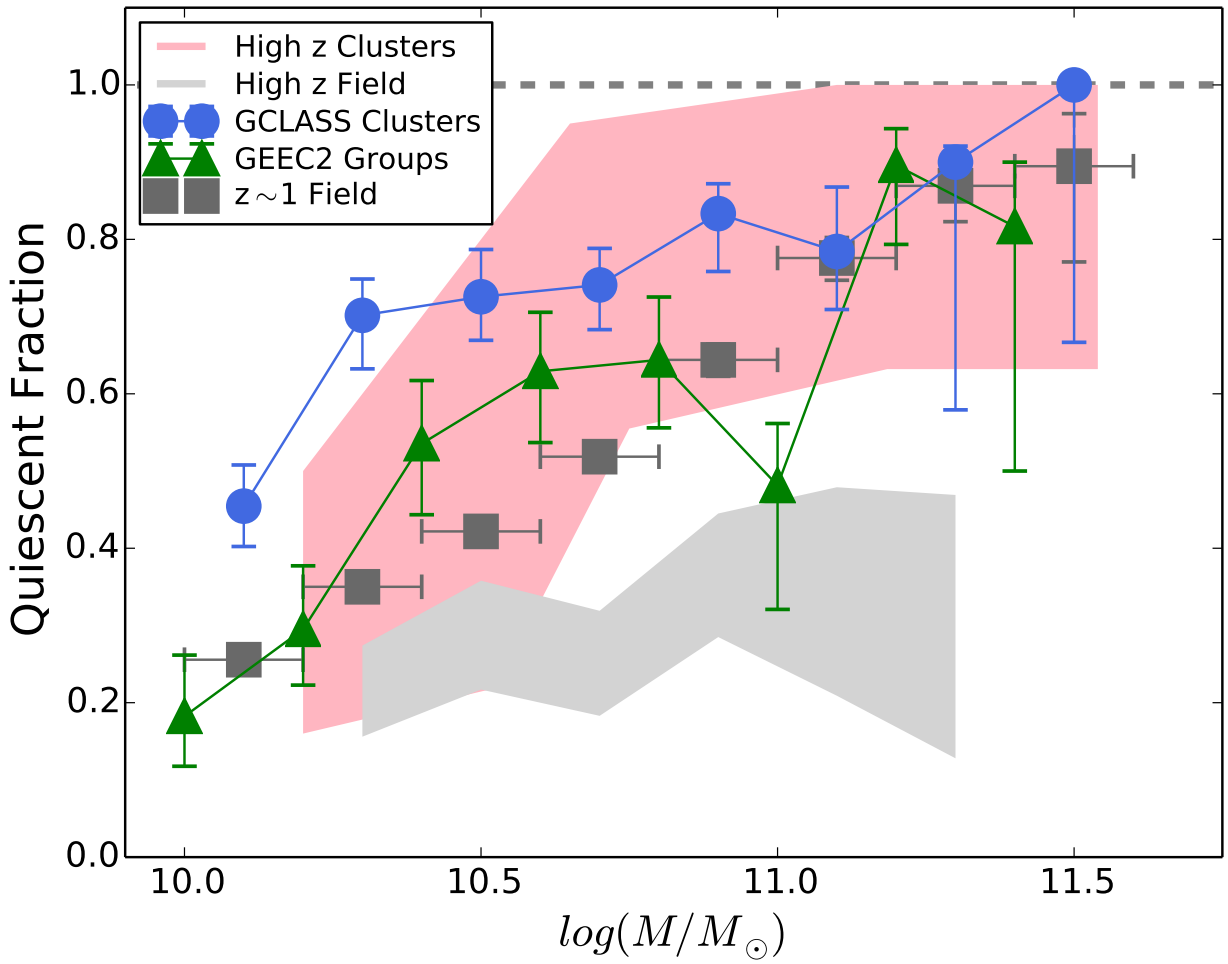

Figure 3.7: The quiescent fraction of galaxies as a function of stellar mass from the GEEC2 group and GCLASS cluster samples (Balogh et al., 2016) at $z \sim 1$. The field sample (gray squares) here is from the $z \sim 1$ sample of van der Burg et al. (2013). Horizontal error bars span mass bin widths, and vertical error bars are from binomial counting statistics. The background shaded regions correspond to the envelopes traced out by the 68% binomial confidence limits for the higher-redshift dense environment (light red) and field (gray) samples from Figure 3.6. Between $z \sim 1.6$ and $z \sim 1$, the value of f_Q in the field dramatically increases for stellar masses above $M_* \sim 10^{10.5} M_\odot$. However, f_Q for the dense environment at $z \sim 1.6$ is consistent with that observed at $z \sim 1$.

Evidence for early cluster red sequence formation at high stellar masses is observed in the ~ 1 GCLASS sample as well (Muzzin et al., 2012). Most of the GCLASS galaxies have $D_n(4000)$ consistent with very old stellar populations, in many cases approaching the age of the Universe at $z = 1$.

However, within our uncertainties, we cannot rule out a mild relation between $D_n(4000)$ and

stellar mass corresponding to a range in z_f of 1 Gyr. Such a trend would be consistent with the results given by Muzzin et al. (2012), who found an increase in $D_n(4000)$ as a function of stellar mass for quiescent cluster galaxies at $z \sim 1$, with $\Delta D_n(4000) \sim 0.2$ over the mass range $10^{9.7} M_\odot \leq M_* \leq 10^{11.1} M_\odot$. The case for older stellar populations in more massive quiescent cluster galaxies has been made by other studies, as well (e.g. Rosati et al. 2009; Jørgensen & Chiboucas 2013; Tanaka et al. 2013). Studies of $D_n(4000)$ in more dense environments over this redshift range should make such a relation apparent, if one exists.

We do note that the weighted mean $D_n(4000)$ for the red sequence galaxies in the protocluster is the same as the value found in our field sample. With the caveat that our field sample only contains two quiescent galaxies which may themselves be in dense environments (e.g., groups), this result is consistent with the suggestion by Newman et al. (2014) that, at least at high galaxy masses and the redshifts of these dense environments, quenching efficiency may be impacted while quenching epoch remains unchanged. That is, the elevated quiescent fraction in IRC 0218 above $M_* = 10^{10.8} M_\odot$ is environmental in origin, but whatever mechanism truncated star formation in these galaxies did not do so earlier than field galaxies of the same masses. However, such a mechanism is as-yet unknown.

Another explanation for the lack of relation between $D_n(4000)$ and stellar mass may be prior or ongoing merging. IRC 0218 does show evidence for an enhanced merger rate, predominantly due to dry (gasless) merging (Lotz et al., 2013). It is important to note that dry merging would merely redistribute red sequence mass, as opposed to the scenario suggested by Brodwin et al. (2013) for lower-redshift ($z \sim 1.3$) clusters, where gas-rich merging fuels AGN feedback and subsequent quenching. Thus, dry merging activity in IRC 0218 may have masked a previously existing trend in $D_n(4000)$ without changing the total mass on the red sequence. Future work is needed to investigate the possible impacts of dry merging through morphological examination of the IRC 0218 red sequence down to our mass completeness limit.

Regardless of whether the absence of relation between $D_n(4000)$ and stellar mass is due to the dominant high-redshift quenching mechanism in the protocluster or the impact of dry merging,

we have shown that the red sequence in IRC 0218 was populated at a very early epoch. This places constraints on possible quenching mechanisms; any possible mechanism would need to be capable of truncating star formation rapidly by $z \sim 3$. This disfavors quenching mechanisms operating on long timescales (e.g., delayed quenching or strangulation, Wetzel et al., 2013; Peng et al., 2015), and favors more abrupt mechanisms (e.g., luminous AGN feedback, Bongiorno et al., 2016). Further constraint of the mechanism responsible for creating the red sequence in IRC 0218 at $z \sim 3.0$ will require observations of dense environments at that epoch.

Chapter 4

Conclusion

We present the results of a study of the quiescent and star forming galaxies in the $z = 1.62$ protocluster IRC 0218, down to stellar masses $M_* = 10^{10.2} M_\odot$. Using IR photometry, *Hubble*/WFC3 grism spectroscopy of the rest-frame 4000 Å break, and a mixture of spectroscopic and grism redshifts, we classified galaxies in the protocluster and field as star forming or quiescent based on their rest-frame $(U-V)$ and $(V-J)$ colors. Stellar masses were estimated through template fitting, and the spectroscopic index $D_n(4000)$ was measured for each galaxy.

Considering all cluster galaxies above our mass completeness limit of $M_* = 10^{10.2} M_\odot$, we find that the quiescent fraction in IRC 0218 is $2-3\times$ higher than a comparable-redshift field sample over a similar range in mass. For protocluster galaxies with $M_* \geq 10^{10.8} M_\odot$, the quiescent fraction is $f_Q = 1.0^{0.00}_{-0.36}$, $2-3\times$ higher than the field fraction, $f_Q = 0.34^{+0.06}_{-0.05}$. However for protocluster galaxies with masses $10^{10.2} M_\odot \leq M_* \leq 10^{10.8} M_\odot$, the quenched fraction is $f_Q = 0.4^{+0.20}_{-0.18}$, comparable to the value in the field, which we find to be $f_Q = 0.24^{+0.04}_{-0.03}$. The results at the high stellar mass end agree with both similar high-redshift clusters as well as likely descendents at $z \sim 1$, indicating that the high quiescent fraction of galaxies in dense environments is already in place at $z = 1.5-1.8$. For the low stellar mass end, comparing IRC 0218 with likely descendents at $z \sim 1$ indicates that f_Q may increase modestly between the two epochs.

We do not find a significant relation between $D_n(4000)$ and stellar mass for quiescent protoclus-

ter galaxies with masses $10^{10.2} M_\odot \leq M_* \leq 10^{11.5} M_\odot$. This suggests that the quiescent galaxies in IRC 0218 shut off star formation at approximately the same time in the redshift range $2.3 \leq z_f \leq 3$, and that the relation between f_Q and stellar mass was imprinted at the time the protocluster red sequence formed. Alternatively, the lack of relation between $D_n(4000)$ and stellar mass may be indicative of mass redistribution in protocluster galaxies through dry merging. In either case, the red sequence in IRC 0218 was already beginning to be populated at $z \sim 3$, placing important constraints on possible quenching mechanisms.

References

Alberts, S., Pope, A., Brodwin, M., Atlee, D. W., Lin, Y.-T., Dey, A., Eisenhardt, P. R. M., Gettings, D. P., Gonzalez, A. H., Jannuzi, B. T., Mancone, C. L., Moustakas, J., Snyder, G. F., Stanford, S. A., Stern, D., Weiner, B. J., & Zeimann, G. R. (2014). The evolution of dust-obscured star formation activity in galaxy clusters relative to the field over the last 9 billion years. *MNRAS*, 437, 437–457.

Andreon, S., Maughan, B., Trinchieri, G., & Kurk, J. (2009). JKCS 041: a colour-detected galaxy cluster at z_{phot} ˜ 1.9 with deep potential well as confirmed by X-ray data. *A&A*, 507, 147–157.

Balogh, M., Eke, V., Miller, C., Lewis, I., Bower, R., Couch, W., Nichol, R., Bland-Hawthorn, J., Baldry, I. K., Baugh, C., Bridges, T., Cannon, R., Cole, S., Colless, M., Collins, C., Cross, N., Dalton, G., de Propris, R., Driver, S. P., Efstathiou, G., Ellis, R. S., Frenk, C. S., Glazebrook, K., Gomez, P., Gray, A., Hawkins, E., Jackson, C., Lahav, O., Lumsden, S., Maddox, S., Madgwick, D., Norberg, P., Peacock, J. A., Percival, W., Peterson, B. A., Sutherland, W., & Taylor, K. (2004). Galaxy ecology: groups and low-density environments in the SDSS and 2dFGRS. *MNRAS*, 348, 1355–1372.

Balogh, M. L., McGee, S. L., Mok, A., Muzzin, A., van der Burg, R. F. J., Bower, R. G., Finoguenov, A., Hoekstra, H., Lidman, C., Mulchaey, J. S., Noble, A., Parker, L. C., Tanaka, M., Wilman, D. J., Webb, T., Wilson, G., & Yee, H. K. C. (2016). Evidence for a change in the dominant satellite galaxy quenching mechanism at z = 1. *MNRAS*, 456, 4364–4376.

Balogh, M. L., Morris, S. L., Yee, H. K. C., Carlberg, R. G., & Ellingson, E. (1999). Differential Galaxy Evolution in Cluster and Field Galaxies at z˜0.3. *ApJ*, 527, 54–79.

Bassett, R., Papovich, C., Lotz, J. M., Bell, E. F., Finkelstein, S. L., Newman, J. A., Tran, K.-V., Almaini, O., Lani, C., Cooper, M., Croton, D., Dekel, A., Ferguson, H. C., Kocevski, D. D., Koekemoer, A. M., Koo, D. C., McGrath, E. J., McIntosh, D. H., & Wechsler, R. (2013). CANDELS Observations of the Environmental Dependence of the Color-Mass-Morphology Relation at z = 1.6. *ApJ*, 770, 58.

Bongiorno, A., Schulze, A., Merloni, A., Zamorani, G., Ilbert, O., La Franca, F., Peng, Y., Piconcelli, E., Mainieri, V., Silverman, J. D., Brusa, M., Fiore, F., Salvato, M., & Scoville, N. (2016). AGN host galaxy mass function in COSMOS. Is AGN feedback responsible for the mass-quenching of galaxies? *A&A*, 588, A78.

Brammer, G. B., van Dokkum, P. G., Franx, M., Fumagalli, M., Patel, S., Rix, H.-W., Skelton, R. E., Kriek, M., Nelson, E., Schmidt, K. B., Bezanson, R., da Cunha, E., Erb, D. K., Fan, X., Förster Schreiber, N., Illingworth, G. D., Labbé, I., Leja, J., Lundgren, B., Magee, D., Marchesini, D., McCarthy, P., Momcheva, I., Muzzin, A., Quadri, R., Steidel, C. C., Tal, T., Wake, D., Whitaker, K. E., & Williams, A. (2012). 3D-HST: A Wide-field Grism Spectroscopic Survey with the Hubble Space Telescope. *ApJS*, 200, 13.

Brodwin, M., Stanford, S. A., Gonzalez, A. H., Zeimann, G. R., Snyder, G. F., Mancone, C. L., Pope, A., Eisenhardt, P. R., Stern, D., Alberts, S., Ashby, M. L. N., Brown, M. J. I., Chary, R.-R., Dey, A., Galametz, A., Gettings, D. P., Jannuzi, B. T., Miller, E. D., Moustakas, J., & Moustakas, L. A. (2013). The Era of Star Formation in Galaxy Clusters. *ApJ*, 779, 138.

Bruzual, G. & Charlot, S. (2003). Stellar population synthesis at the resolution of 2003. *MNRAS*, 344, 1000–1028.

Bruzual A., G. (1983). Spectral evolution of galaxies. I - Early-type systems. *ApJ*, 273, 105–127.

Calzetti, D., Armus, L., Bohlin, R. C., Kinney, A. L., Koornneef, J., & Storchi-Bergmann, T. (2000). The Dust Content and Opacity of Actively Star-forming Galaxies. *ApJ*, 533, 682–695.

Chabrier, G. (2003). Galactic Stellar and Substellar Initial Mass Function. *PASP*, 115, 763–795.

Cooke, E. A., Hatch, N. A., Stern, D., Rettura, A., Brodwin, M., Galametz, A., Wylezalek, D., Bridge, C., Conselice, C. J., De Breuck, C., Gonzalez, A. H., & Jarvis, M. (2016). A Mature Galaxy Cluster at z=1.58 around the Radio Galaxy 7C1753+6311. *ApJ*, 816, 83.

Delaye, L., Huertas-Company, M., Mei, S., Lidman, C., Licitra, R., Newman, A., Raichoor, A., Shankar, F., Barrientos, F., Bernardi, M., Cerulo, P., Couch, W., Demarco, R., Muñoz, R., Sánchez-Janssen, R., & Tanaka, M. (2014). Larger sizes of massive quiescent early-type galaxies in clusters than in the field at 0.8 z 1.5. *MNRAS*, 441, 203–223.

Fassbender, R., Nastasi, A., Santos, J. S., Lidman, C., Verdugo, M., Koyama, Y., Rosati, P., Pierini, D., Padilla, N., Romeo, A. D., Menci, N., Bongiorno, A., Castellano, M., Cerulo, P., Fontana, A., Galametz, A., Grazian, A., Lamastra, A., Pentericci, L., Sommariva, V., Strazzullo, V., Šuhada, R., & Tozzi, P. (2014). Galaxy population properties of the massive X-ray luminous galaxy cluster <ASTROBJ>XDCP J0044.0-2033</ASTROBJ> at z = 1.58. Red-sequence formation, massive galaxy assembly, and central star formation activity. *A&A*, 568, A5.

Finoguenov, A., Watson, M. G., Tanaka, M., Simpson, C., Cirasuolo, M., Dunlop, J. S., Peacock, J. A., Farrah, D., Akiyama, M., Ueda, Y., Smolčić, V., Stewart, G., Rawlings, S., van Breukelen, C., Almaini, O., Clewley, L., Bonfield, D. G., Jarvis, M. J., Barr, J. M., Foucaud, S., McLure, R. J., Sekiguchi, K., & Egami, E. (2010). X-ray groups and clusters of galaxies in the Subaru-XMM Deep Field. *MNRAS*, 403, 2063–2076.

Gehrels, N. (1986). Confidence limits for small numbers of events in astrophysical data. *ApJ*, 303, 336–346.

Gobat, R., Daddi, E., Onodera, M., Finoguenov, A., Renzini, A., Arimoto, N., Bouwens, R., Brusa, M., Chary, R.-R., Cimatti, A., Dickinson, M., Kong, X., & Mignoli, M. (2011). A mature cluster with X-ray emission at z = 2.07. *A&A*, 526, A133.

Gómez, P. L., Nichol, R. C., Miller, C. J., Balogh, M. L., Goto, T., Zabludoff, A. I., Romer, A. K., Bernardi, M., Sheth, R., Hopkins, A. M., Castander, F. J., Connolly, A. J., Schneider, D. P., Brinkmann, J., Lamb, D. Q., SubbaRao, M., & York, D. G. (2003). Galaxy Star Formation as a Function of Environment in the Early Data Release of the Sloan Digital Sky Survey. *ApJ*, 584, 210–227.

Grogin, N. A., Kocevski, D. D., Faber, S. M., Ferguson, H. C., Koekemoer, A. M., Riess, A. G., Acquaviva, V., Alexander, D. M., Almaini, O., Ashby, M. L. N., Barden, M., Bell, E. F., Bournaud, F., Brown, T. M., Caputi, K. I., Casertano, S., Cassata, P., Castellano, M., Challis, P., Chary, R.-R., Cheung, E., Cirasuolo, M., Conselice, C. J., Roshan Cooray, A., Croton, D. J., Daddi, E., Dahlen, T., Davé, R., de Mello, D. F., Dekel, A., Dickinson, M., Dolch, T., Donley, J. L., Dunlop, J. S., Dutton, A. A., Elbaz, D., Fazio, G. G., Filippenko, A. V., Finkelstein, S. L., Fontana, A., Gardner, J. P., Garnavich, P. M., Gawiser, E., Giavalisco, M., Grazian, A., Guo, Y., Hathi, N. P., Häussler, B., Hopkins, P. F., Huang, J.-S., Huang, K.-H., Jha, S. W., Kartaltepe, J. S., Kirshner, R. P., Koo, D. C., Lai, K., Lee, K.-S., Li, W., Lotz, J. M., Lucas, R. A., Madau, P., McCarthy, P. J., McGrath, E. J., McIntosh, D. H., McLure, R. J., Mobasher, B., Moustakas, L. A., Mozena, M., Nandra, K., Newman, J. A., Niemi, S.-M., Noeske, K. G., Papovich, C. J., Pentericci, L., Pope, A., Primack, J. R., Rajan, A., Ravindranath, S., Reddy, N. A., Renzini, A., Rix, H.-W., Robaina, A. R., Rodney, S. A., Rosario, D. J., Rosati, P., Salimbeni, S., Scarlata, C., Siana, B., Simard, L., Smidt, J., Somerville, R. S., Spinrad, H., Straughn, A. N., Strolger, L.-G., Telford, O., Teplitz, H. I., Trump, J. R., van der Wel, A., Villforth, C., Wechsler, R. H., Weiner, B. J., Wiklind, T., Wild, V., Wilson, G., Wuyts, S., Yan, H.-J., & Yun, M. S. (2011). CANDELS: The Cosmic Assembly Near-infrared Deep Extragalactic Legacy Survey. *ApJS*, 197, 35.

Hashimoto, Y., Oemler, Jr., A., Lin, H., & Tucker, D. L. (1998). The Influence of Environment on the Star Formation Rates of Galaxies. *ApJ*, 499, 589–599.

Hatch, N. A., Muldrew, S. I., Cooke, E. A., Hartley, W. G., Almaini, O., Simpson, C. J., & Conselice, C. J. (2016). The structure and evolution of a forming galaxy cluster at z = 1.62. *MNRAS*, 459, 387–401.

Henke, B. (2015). Measuring D(4000) in $z \sim 1.6$ Galaxies Using WFC3/G102L Observations with *HST*: A Feasibility Study. Master's thesis, The University of Kansas, Lawrence, KS, USA.

Hilton, M., Stanford, S. A., Stott, J. P., Collins, C. A., Hoyle, B., Davidson, M., Hosmer, M., Kay, S. T., Liddle, A. R., Lloyd-Davies, E., Mann, R. G., Mehrtens, N., Miller, C. J., Nichol, R. C., Romer, A. K., Sabirli, K., Sahlén, M., Viana, P. T. P., West, M. J., Barbary, K., Dawson, K. S., Meyers, J., Perlmutter, S., Rubin, D., & Suzuki, N. (2009). The XMM Cluster Survey: Galaxy Morphologies and the Color-Magnitude Relation in XMMXCS J2215.9 - 1738 at z = 1.46. *ApJ*, 697, 436–451.

Hogg, D. W., Blanton, M. R., Brinchmann, J., Eisenstein, D. J., Schlegel, D. J., Gunn, J. E., McKay, T. A., Rix, H.-W., Bahcall, N. A., Brinkmann, J., & Meiksin, A. (2004). The Dependence on Environment of the Color-Magnitude Relation of Galaxies. *ApJ*, 601, L29–L32.

Horne, K. (1986). An optimal extraction algorithm for CCD spectroscopy. *PASP*, 98, 609–617.

Jørgensen, I. & Chiboucas, K. (2013). Stellar Populations and Evolution of Early-type Cluster Galaxies: Constraints from Optical Imaging and Spectroscopy of z = 0.5-0.9 Galaxy Clusters. *AJ*, 145, 77.

Kauffmann, G., Heckman, T. M., White, S. D. M., Charlot, S., Tremonti, C., Peng, E. W., Seibert, M., Brinkmann, J., Nichol, R. C., SubbaRao, M., & York, D. (2003). The dependence of star formation history and internal structure on stellar mass for 10^5 low-redshift galaxies. *MNRAS*, 341, 54–69.

Koekemoer, A. M., Faber, S. M., Ferguson, H. C., Grogin, N. A., Kocevski, D. D., Koo, D. C., Lai, K., Lotz, J. M., Lucas, R. A., McGrath, E. J., Ogaz, S., Rajan, A., Riess, A. G., Rodney, S. A., Strolger, L., Casertano, S., Castellano, M., Dahlen, T., Dickinson, M., Dolch, T., Fontana, A., Giavalisco, M., Grazian, A., Guo, Y., Hathi, N. P., Huang, K.-H., van der Wel, A., Yan, H.-J., Acquaviva, V., Alexander, D. M., Almaini, O., Ashby, M. L. N., Barden, M., Bell, E. F., Bournaud, F., Brown, T. M., Caputi, K. I., Cassata, P., Challis, P. J., Chary, R.-R., Cheung, E., Cirasuolo, M., Conselice, C. J., Roshan Cooray, A., Croton, D. J., Daddi, E., Davé, R., de Mello, D. F., de Ravel, L., Dekel, A., Donley, J. L., Dunlop, J. S., Dutton, A. A., Elbaz, D., Fazio, G. G., Filippenko, A. V., Finkelstein, S. L., Frazer, C., Gardner, J. P., Garnavich, P. M., Gawiser, E., Gruetzbauch, R., Hartley, W. G., Häussler, B., Herrington, J., Hopkins, P. F., Huang, J.-S., Jha, S. W., Johnson, A., Kartaltepe, J. S., Khostovan, A. A., Kirshner, R. P., Lani, C., Lee, K.-S., Li, W., Madau, P., McCarthy, P. J., McIntosh, D. H., McLure, R. J., McPartland, C., Mobasher, B., Moreira, H., Mortlock, A., Moustakas, L. A., Mozena, M., Nandra, K., Newman, J. A., Nielsen, J. L., Niemi, S., Noeske, K. G., Papovich, C. J., Pentericci, L., Pope, A., Primack, J. R., Ravindranath, S., Reddy, N. A., Renzini, A., Rix, H.-W., Robaina, A. R., Rosario, D. J., Rosati, P., Salimbeni, S., Scarlata, C., Siana, B., Simard, L., Smidt, J., Snyder, D., Somerville, R. S., Spinrad, H., Straughn, A. N., Telford, O., Teplitz, H. I., Trump, J. R., Vargas, C., Villforth, C., Wagner, C. R., Wandro, P., Wechsler, R. H., Weiner, B. J., Wiklind, T., Wild, V., Wilson, G., Wuyts, S., & Yun, M. S. (2011). CANDELS: The Cosmic Assembly Near-infrared Deep Extragalactic Legacy SurveyThe Hubble Space Telescope Observations, Imaging Data Products, and Mosaics. *ApJS*, 197, 36.

Kriek, M., van der Wel, A., van Dokkum, P. G., Franx, M., & Illingworth, G. D. (2008). The Detection of a Red Sequence of Massive Field Galaxies at z ˜ 2.3 and Its Evolution to z ˜ 0. *ApJ*, 682, 896–906.

Kriek, M., van Dokkum, P. G., Labbé, I., Franx, M., Illingworth, G. D., Marchesini, D., & Quadri, R. F. (2009). An Ultra-Deep Near-Infrared Spectrum of a Compact Quiescent Galaxy at z = 2.2.

ApJ, 700, 221–231.

Lawrence, A., Warren, S. J., Almaini, O., Edge, A. C., Hambly, N. C., Jameson, R. F., Lucas, P., Casali, M., Adamson, A., Dye, S., Emerson, J. P., Foucaud, S., Hewett, P., Hirst, P., Hodgkin, S. T., Irwin, M. J., Lodieu, N., McMahon, R. G., Simpson, C., Smail, I., Mortlock, D., & Folger, M. (2007). The UKIRT Infrared Deep Sky Survey (UKIDSS). *MNRAS*, 379, 1599–1617.

Lee, S.-K., Im, M., Kim, J.-W., Lotz, J., McPartland, C., Peth, M., & Koekemoer, A. (2015). Evolution of Star-formation Properties of High-redshift Cluster Galaxies since z = 2. *ApJ*, 810, 90.

Lewis, I., Balogh, M., De Propris, R., Couch, W., Bower, R., Offer, A., Bland-Hawthorn, J., Baldry, I. K., Baugh, C., Bridges, T., Cannon, R., Cole, S., Colless, M., Collins, C., Cross, N., Dalton, G., Driver, S. P., Efstathiou, G., Ellis, R. S., Frenk, C. S., Glazebrook, K., Hawkins, E., Jackson, C., Lahav, O., Lumsden, S., Maddox, S., Madgwick, D., Norberg, P., Peacock, J. A., Percival, W., Peterson, B. A., Sutherland, W., & Taylor, K. (2002). The 2dF Galaxy Redshift Survey: the environmental dependence of galaxy star formation rates near clusters. *MNRAS*, 334, 673–683.

Lotz, J. M., Papovich, C., Faber, S. M., Ferguson, H. C., Grogin, N., Guo, Y., Kocevski, D., Koekemoer, A. M., Lee, K.-S., McIntosh, D., Momcheva, I., Rudnick, G., Saintonge, A., Tran, K.-V., van der Wel, A., & Willmer, C. (2013). Caught in the Act: The Assembly of Massive Cluster Galaxies at z = 1.62. *ApJ*, 773, 154.

Marchesini, D., van Dokkum, P. G., Förster Schreiber, N. M., Franx, M., Labbé, I., & Wuyts, S. (2009). The Evolution of the Stellar Mass Function of Galaxies from z = 4.0 and the First Comprehensive Analysis of its Uncertainties: Evidence for Mass-Dependent Evolution. *ApJ*, 701, 1765–1796.

Mei, S., Holden, B. P., Blakeslee, J. P., Ford, H. C., Franx, M., Homeier, N. L., Illingworth, G. D., Jee, M. J., Overzier, R., Postman, M., Rosati, P., Van der Wel, A., & Bartlett, J. G.

(2009). Evolution of the Color-Magnitude Relation in Galaxy Clusters at z ˜ 1 from the ACS Intermediate Redshift Cluster Survey. *ApJ*, 690, 42–68.

Mei, S., Scarlata, C., Pentericci, L., Newman, J. A., Weiner, B. J., Ashby, M. L. N., Castellano, M., Conselice, C. J., Finkelstein, S. L., Galametz, A., Grogin, N. A., Koekemoer, A. M., Huertas-Company, M., Lani, C., Lucas, R. A., Papovich, C., Rafelski, M., & Teplitz, H. I. (2015). Star-forming Blue ETGs in Two Newly Discovered Galaxy Overdensities in the HUDF at z=1.84 and 1.9: Unveiling the Progenitors of Passive ETGs in Cluster Cores. *ApJ*, 804, 117.

Momcheva, I. G., Brammer, G. B., van Dokkum, P. G., Skelton, R. E., Whitaker, K. E., Nelson, E. J., Fumagalli, M., Maseda, M. V., Leja, J., Franx, M., Rix, H.-W., Bezanson, R., Da Cunha, E., Dickey, C., Förster Schreiber, N. M., Illingworth, G., Kriek, M., Labbé, I., Ulf Lange, J., Lundgren, B. F., Magee, D., Marchesini, D., Oesch, P., Pacifici, C., Patel, S. G., Price, S., Tal, T., Wake, D. A., van der Wel, A., & Wuyts, S. (2016). The 3D-HST Survey: Hubble Space Telescope WFC3/G141 Grism Spectra, Redshifts, and Emission Line Measurements for ˜ 100,000 Galaxies. *ApJS*, 225, 27.

Muzzin, A., Wilson, G., Yee, H. K. C., Gilbank, D., Hoekstra, H., Demarco, R., Balogh, M., van Dokkum, P., Franx, M., Ellingson, E., Hicks, A., Nantais, J., Noble, A., Lacy, M., Lidman, C., Rettura, A., Surace, J., & Webb, T. (2012). The Gemini Cluster Astrophysics Spectroscopic Survey (GCLASS): The Role of Environment and Self-regulation in Galaxy Evolution at z ˜ 1. *ApJ*, 746, 188.

Nantais, J. B., van der Burg, R. F. J., Lidman, C., Demarco, R., Noble, A., Wilson, G., Muzzin, A., Foltz, R., DeGroot, A., & Cooper, M. C. (2016). Stellar mass function of cluster galaxies at z ˜ 1.5: evidence for reduced quenching efficiency at high redshift. *A&A*, 592, A161.

Newman, A. B., Ellis, R. S., Andreon, S., Treu, T., Raichoor, A., & Trinchieri, G. (2014). Spectroscopic Confirmation of the Rich z = 1.80 Galaxy Cluster JKCS 041 using the WFC3 Grism: Environmental Trends in the Ages and Structure of Quiescent Galaxies. *ApJ*, 788, 51.

Papovich, C., Bassett, R., Lotz, J. M., van der Wel, A., Tran, K.-V., Finkelstein, S. L., Bell, E. F., Conselice, C. J., Dekel, A., Dunlop, J. S., Guo, Y., Faber, S. M., Farrah, D., Ferguson, H. C., Finkelstein, K. D., Häussler, B., Kocevski, D. D., Koekemoer, A. M., Koo, D. C., McGrath, E. J., McLure, R. J., McIntosh, D. H., Momcheva, I., Newman, J. A., Rudnick, G., Weiner, B., Willmer, C. N. A., & Wuyts, S. (2012). CANDELS Observations of the Structural Properties of Cluster Galaxies at z = 1.62. *ApJ*, 750, 93.

Papovich, C., Momcheva, I., Willmer, C. N. A., Finkelstein, K. D., Finkelstein, S. L., Tran, K.-V., Brodwin, M., Dunlop, J. S., Farrah, D., Khan, S. A., Lotz, J., McCarthy, P., McLure, R. J., Rieke, M., Rudnick, G., Sivanandam, S., Pacaud, F., & Pierre, M. (2010). A Spitzer-selected Galaxy Cluster at z = 1.62. *ApJ*, 716, 1503–1513.

Patel, S. G., Holden, B. P., Kelson, D. D., Illingworth, G. D., & Franx, M. (2009). The Dependence of Star Formation Rates on Stellar Mass and Environment at z ˜ 0.8. *ApJ*, 705, L67–L70.

Peng, Y., Maiolino, R., & Cochrane, R. (2015). Strangulation as the primary mechanism for shutting down star formation in galaxies. *Nature*, 521, 192–195.

Pierre, M., Clerc, N., Maughan, B., Pacaud, F., Papovich, C., & Willmer, C. N. A. (2012). A Chandra view of the z = 1.62 galaxy cluster IRC-0218A. *A&A*, 540, A4.

Quadri, R. F., Williams, R. J., Franx, M., & Hildebrandt, H. (2012). Tracing the Star-formation-Density Relation to z ˜ 2. *ApJ*, 744, 88.

Rosati, P., Tozzi, P., Gobat, R., Santos, J. S., Nonino, M., Demarco, R., Lidman, C., Mullis, C. R., Strazzullo, V., Böhringer, H., Fassbender, R., Dawson, K., Tanaka, M., Jee, J., Ford, H., Lamer, G., & Schwope, A. (2009). Multi-wavelength study of XMMU J2235.3-2557: the most massive galaxy cluster at z 1. *A&A*, 508, 583–591.

Rudnick, G., Rix, H.-W., & Kennicutt, Jr., R. C. (2000). Lopsided Galaxies, Weak Interactions, and Boosting the Star Formation Rate. *ApJ*, 538, 569–580.

Rudnick, G. H., Tran, K.-V., Papovich, C., Momcheva, I., & Willmer, C. (2012). A Tale of Dwarfs and Giants: Using a z = 1.62 Cluster to Understand How the Red Sequence Grew over the Last 9.5 Billion Years. *ApJ*, 755, 14.

Santos, J. S., Fassbender, R., Nastasi, A., Böhringer, H., Rosati, P., Šuhada, R., Pierini, D., Nonino, M., Mühlegger, M., Quintana, H., Schwope, A. D., Lamer, G., de Hoon, A., & Strazzullo, V. (2011). Discovery of a massive X-ray luminous galaxy cluster at z = 1.579. *A&A*, 531, L15.

Skelton, R. E., Whitaker, K. E., Momcheva, I. G., Brammer, G. B., van Dokkum, P. G., Labbé, I., Franx, M., van der Wel, A., Bezanson, R., Da Cunha, E., Fumagalli, M., Förster Schreiber, N., Kriek, M., Leja, J., Lundgren, B. F., Magee, D., Marchesini, D., Maseda, M. V., Nelson, E. J., Oesch, P., Pacifici, C., Patel, S. G., Price, S., Rix, H.-W., Tal, T., Wake, D. A., & Wuyts, S. (2014). 3D-HST WFC3-selected Photometric Catalogs in the Five CANDELS/3D-HST Fields: Photometry, Photometric Redshifts, and Stellar Masses. *ApJS*, 214, 24.

Stanford, S. A., Brodwin, M., Gonzalez, A. H., Zeimann, G., Stern, D., Dey, A., Eisenhardt, P. R., Snyder, G. F., & Mancone, C. (2012). IDCS J1426.5+3508: Discovery of a Massive, Infrared-selected Galaxy Cluster at z = 1.75. *ApJ*, 753, 164.

Straatman, C. M. S., Labbé, I., Spitler, L. R., Allen, R., Altieri, B., Brammer, G. B., Dickinson, M., van Dokkum, P., Inami, H., Glazebrook, K., Kacprzak, G. G., Kawinwanichakij, L., Kelson, D. D., McCarthy, P. J., Mehrtens, N., Monson, A., Murphy, D., Papovich, C., Persson, S. E., Quadri, R., Rees, G., Tomczak, A., Tran, K.-V. H., & Tilvi, V. (2014). A Substantial Population of Massive Quiescent Galaxies at z ˜ 4 from ZFOURGE. *ApJ*, 783, L14.

Tadaki, K.-i., Kodama, T., Ota, K., Hayashi, M., Koyama, Y., Papovich, C., Brodwin, M., Tanaka, M., & Iye, M. (2012). A large-scale structure traced by [O II] emitters hosting a distant cluster at z= 1.62. *MNRAS*, 423, 2617–2626.

Tal, T., Dekel, A., Oesch, P., Muzzin, A., Brammer, G. B., van Dokkum, P. G., Franx, M., Illingworth, G. D., Leja, J., Magee, D., Marchesini, D., Momcheva, I., Nelson, E. J., Patel, S. G.,

Quadri, R. F., Rix, H.-W., Skelton, R. E., Wake, D. A., & Whitaker, K. E. (2014). Observations of Environmental Quenching in Groups in the 11 GYR since z = 2.5: Different Quenching for Central and Satellite Galaxies. *ApJ*, 789, 164.

Tanaka, M., Finoguenov, A., & Ueda, Y. (2010). A Spectroscopically Confirmed X-ray Cluster at z = 1.62 with a Possible Companion in the Subaru/XMM-Newton Deep Field. *ApJ*, 716, L152–L156.

Tanaka, M., Toft, S., Marchesini, D., Zirm, A., De Breuck, C., Kodama, T., Koyama, Y., Kurk, J., & Tanaka, I. (2013). On the Formation Timescale of Massive Cluster Ellipticals Based on Deep Near-infrared Spectroscopy at z ˜ 2. *ApJ*, 772, 113.

Tran, K.-V. H., Nanayakkara, T., Yuan, T., Kacprzak, G. G., Glazebrook, K., Kewley, L. J., Momcheva, I., Papovich, C. J., Quadri, R., Rudnick, G., Saintonge, A., Spitler, L. R., Straatman, C., & Tomczak, A. (2015). ZFIRE: Galaxy Cluster Kinematics, H alpha Star Formation Rates, and Gas Phase Metallicities of XMM-LSS J02182-05102 at zcl = 1.6232. *ApJ*, 811, 28.

Tran, K.-V. H., Papovich, C., Saintonge, A., Brodwin, M., Dunlop, J. S., Farrah, D., Finkelstein, K. D., Finkelstein, S. L., Lotz, J., McLure, R. J., Momcheva, I., & Willmer, C. N. A. (2010). Reversal of Fortune: Confirmation of an Increasing Star Formation-Density Relation in a Cluster at z = 1.62. *ApJ*, 719, L126–L129.

van der Burg, R. F. J., Muzzin, A., Hoekstra, H., Lidman, C., Rettura, A., Wilson, G., Yee, H. K. C., Hildebrandt, H., Marchesini, D., Stefanon, M., Demarco, R., & Kuijken, K. (2013). The environmental dependence of the stellar mass function at z ˜ 1. Comparing cluster and field between the GCLASS and UltraVISTA surveys. *A&A*, 557, A15.

Wetzel, A. R., Tinker, J. L., Conroy, C., & van den Bosch, F. C. (2013). Galaxy evolution in groups and clusters: satellite star formation histories and quenching time-scales in a hierarchical Universe. *MNRAS*, 432, 336–358.

Whitaker, K. E., van Dokkum, P. G., Brammer, G., & Franx, M. (2012). The Star Formation Mass Sequence Out to z = 2.5. *ApJ*, 754, L29.

Whitaker, K. E., van Dokkum, P. G., Brammer, G., Momcheva, I. G., Skelton, R., Franx, M., Kriek, M., Labbé, I., Fumagalli, M., Lundgren, B. F., Nelson, E. J., Patel, S. G., & Rix, H.-W. (2013). Quiescent Galaxies in the 3D-HST Survey: Spectroscopic Confirmation of a Large Number of Galaxies with Relatively Old Stellar Populations at z ˜ 2. *ApJ*, 770, L39.

Williams, R. J., Quadri, R. F., Franx, M., van Dokkum, P., & Labbé, I. (2009). Detection of Quiescent Galaxies in a Bicolor Sequence from Z = 0-2. *ApJ*, 691, 1879–1895.

Wuyts, S., Labbé, I., Franx, M., Rudnick, G., van Dokkum, P. G., Fazio, G. G., Förster Schreiber, N. M., Huang, J., Moorwood, A. F. M., Rix, H.-W., Röttgering, H., & van der Werf, P. (2007). What Do We Learn from IRAC Observations of Galaxies at 2 z 3.5? *ApJ*, 655, 51–65.

Zeimann, G. R., Stanford, S. A., Brodwin, M., Gonzalez, A. H., Snyder, G. F., Stern, D., Eisenhardt, P., Mancone, C., & Dey, A. (2012). IDCS J1433.2+3306: An Infrared-selected Galaxy Cluster at z = 1.89. *ApJ*, 756, 115.

Appendix A

IRC 0218 and Field Galaxy Properties

A.1 The IRC 0218 and Field Galaxy Grism Samples

Table A.1. IRC 0218 Galaxy Sample

3DHST ID	Q/SF	z	$J_{AB_{rest}}$	$(U-V)_{rest}$	$(V-J)_{rest}$	$log(M/M_{\odot})$	$D_n(4000)$
31684	Q	$1.631^{0.003}_{0.008}$	19.82	1.79	1.15	11.48	$1.56^{0.08}_{0.08}$
30737 [a,b]	Q	1.621	19.60	1.76	1.01	11.26	$1.35^{0.03}_{0.03}$
36010	Q	$1.628^{0.003}_{0.003}$	20.39	1.90	1.25	11.03	$1.32^{0.13}_{0.10}$
29983	Q	$1.629^{0.003}_{0.003}$	20.52	2.14	1.35	10.97	$1.54^{0.12}_{0.13}$
30169 [b]	SF	1.629	20.67	1.64	1.69	10.82	$1.16^{0.32}_{0.23}$
29899	Q	$1.620^{0.005}_{0.006}$	20.98	1.84	1.28	10.77	$2.23^{0.34}_{0.29}$
30545 [a,b]	SF	1.624	20.71	1.54	1.46	10.76	$1.15^{0.12}_{0.12}$
29007	SF	$1.624^{0.004}_{0.005}$	20.84	1.79	1.45	10.65	$1.43^{0.13}_{0.14}$
33092	Q	$1.621^{0.004}_{0.004}$	21.19	1.52	0.68	10.62	$1.49^{0.09}_{0.09}$
32696	SF	$1.625^{0.006}_{0.082}$	21.03	1.63	1.41	10.60	$1.43^{0.29}_{0.18}$
31086 [b]	SF	1.623	21.75	1.40	0.92	10.38	$1.22^{0.16}_{0.15}$
31703 [b,c]	SF	1.623	21.71	0.75	0.83	10.36	$1.14^{0.11}_{0.09}$
28015	Q	$1.620^{0.001}_{0.001}$	21.94	1.61	0.72	10.30	$0.95^{0.44}_{0.32}$
27956	Q	$1.629^{0.063}_{0.214}$	22.17	1.63	0.83	10.27	$1.37^{0.69}_{0.42}$
31715	SF	$1.626^{0.004}_{0.002}$	22.24	0.77	0.82	10.15	$1.23^{0.25}_{0.20}$
30456	SF	$1.610^{0.028}_{0.004}$	21.55	1.54	2.12	10.08	$1.48^{1.90}_{0.89}$
30472 [b]	SF	1.623	22.21	0.68	0.72	10.05	$1.12^{0.09}_{0.10}$
35210	SF	$1.632^{0.013}_{0.220}$	23.11	1.47	1.01	9.87	$1.17^{1.36}_{0.62}$
29841	SF	$1.623^{0.001}_{0.001}$	22.60	0.43	0.58	9.86	$0.91^{0.10}_{0.08}$
33093 [b,c]	SF	1.629	23.06	0.65	0.29	9.63	$1.36^{0.32}_{0.27}$
32608 [b]	SF	1.626	23.19	0.59	0.35	9.55	$0.96^{0.18}_{0.17}$
28036	SF	$1.619^{0.003}_{0.003}$	23.24	0.62	0.07	9.51	$1.30^{0.35}_{0.26}$
29050 [b]	SF	1.624	23.38	0.75	0.54	9.48	$0.62^{0.16}_{0.13}$
33068 [b]	SF	1.624	23.60	0.40	0.11	9.38	$1.12^{0.35}_{0.32}$
30952	SF	$1.629^{0.001}_{0.004}$	24.41	0.47	0.05	8.88	$0.79^{0.34}_{0.23}$

Note. — Redshifts with uncertainty values are 68% intervals derived by bootstrapping over the joint-fit G102+G141+photometry redshift probability distributions. Redshifts without uncertainties are from ground-based spectroscopy, with sources indicated. In cases where multiple ground-based redshifts are available, the average redshift is reported. *References:* (a): Tanaka et al. (2010), (b): Tran et al. (2015), (c): Papovich et al. (2010).

Table A.2. Field Galaxy Sample

3DHST ID	Q/SF	z	$J_{AB_{rest}}$	$(U-V)_{rest}$	$(V-J)_{rest}$	$log(M/M_{\odot})$	$D_n(4000)$
29179	SF	$1.562^{0.007}_{0.010}$	20.25	1.85	1.71	11.21	$2.48^{2.00}_{0.86}$
32904	Q	$1.322^{0.001}_{0.001}$	19.69	1.89	1.15	11.07	$1.42^{0.03}_{0.03}$
32468	SF	$1.308^{0.018}_{0.030}$	20.45	2.23	2.11	11.00	$-0.12^{0.51}_{0.61}$
34899	SF	$1.289^{0.001}_{0.001}$	21.03	0.95	1.43	10.82	$0.87^{0.05}_{0.04}$
33670	SF	$1.416^{0.034}_{0.005}$	20.88	1.87	1.60	10.65	$2.21^{3.79}_{2.57}$
32166	SF	$1.324^{0.004}_{0.003}$	20.79	1.53	1.31	10.58	$1.02^{0.15}_{0.13}$
33472	SF	$1.330^{0.006}_{0.007}$	21.24	1.59	1.24	10.39	$1.59^{0.23}_{0.21}$
28822	Q	$1.756^{0.002}_{0.002}$	21.66	1.34	0.74	10.37	$1.32^{0.09}_{0.10}$
33524	SF	$1.606^{0.010}_{0.233}$	22.21	1.58	1.53	10.35	$1.40^{0.92}_{0.55}$
30994	SF	$1.278^{0.001}_{0.002}$	21.55	1.04	1.23	10.28	$1.13^{0.11}_{0.18}$
34916	SF	$1.539^{0.027}_{0.029}$	21.93	1.23	1.27	10.26	$1.51^{0.25}_{0.34}$
27657	SF	$1.452^{0.007}_{0.008}$	21.86	1.01	0.86	10.24	$1.48^{0.27}_{0.19}$
28211	SF	$1.531^{0.015}_{0.014}$	22.06	1.36	1.70	10.14	$16.78^{36.52}_{17.56}$
29879	SF	$1.670^{0.004}_{0.135}$	22.39	1.56	1.17	10.12	$1.82^{1.63}_{0.91}$
35978	SF	$1.726^{0.238}_{0.088}$	23.10	1.28	0.93	10.08	$1.76^{3.50}_{1.74}$
32931	Q	$1.565^{0.004}_{0.003}$	22.47	1.42	0.69	10.03	$1.11^{0.25}_{0.16}$
31745	SF	$1.507^{0.189}_{0.050}$	22.35	1.27	0.78	10.01	$1.56^{1.37}_{0.68}$
31128	SF	$1.553^{0.001}_{0.001}$	22.21	0.67	0.37	9.95	$0.94^{0.10}_{0.07}$
31079	SF	$1.393^{0.001}_{0.001}$	21.87	0.76	0.71	9.91	$1.11^{0.08}_{0.08}$
36949	SF	$1.665^{0.005}_{0.092}$	22.50	0.69	0.41	9.90	$1.29^{0.22}_{0.12}$
35083	Q	$1.729^{0.038}_{0.028}$	23.09	1.41	0.86	9.89	$1.17^{0.96}_{0.35}$
27454	SF	$1.409^{0.001}_{0.001}$	21.62	1.09	1.69	9.87	$0.47^{0.17}_{0.16}$
33889	SF	$1.539^{0.003}_{0.005}$	22.46	0.64	0.52	9.85	$1.05^{0.11}_{0.10}$
28584	SF	$1.290^{0.001}_{0.007}$	22.36	0.70	0.55	9.80	$1.48^{0.22}_{0.25}$
34940	SF	$1.460^{0.057}_{0.022}$	22.91	1.38	0.89	9.80	$1.32^{0.49}_{0.48}$
31176	Q	$1.554^{0.002}_{0.001}$	23.36	1.65	0.57	9.79	$1.94^{2.31}_{0.93}$
37588	SF	$1.755^{0.002}_{0.002}$	23.10	0.81	0.43	9.71	$1.12^{0.29}_{0.23}$
27068	SF	$1.499^{0.002}_{0.001}$	22.46	0.68	0.54	9.68	$1.26^{0.24}_{0.19}$
33615	SF	$1.719^{0.028}_{0.047}$	23.28	1.13	0.43	9.66	$1.56^{0.60}_{0.61}$
31068	SF	$1.718^{0.004}_{0.040}$	23.60	1.08	0.67	9.66	$0.67^{0.52}_{0.31}$
27102	SF	$1.518^{0.001}_{0.001}$	22.98	0.48	0.78	9.48	$1.56^{0.42}_{0.34}$
35385	SF	$1.316^{0.009}_{0.070}$	23.01	0.67	0.69	9.48	$0.93^{0.36}_{0.16}$
34110	SF	$1.410^{0.002}_{0.002}$	23.27	0.69	0.50	9.46	$1.20^{0.18}_{0.17}$

(continued)

Table A.3. Field Galaxy Sample (continued)

3DHST ID	Q/SF	z	$J_{AB_{rest}}$	$(U-V)_{rest}$	$(V-J)_{rest}$	$log(M/M_{\odot})$	$D_n(4000)$
34110	SF	$1.410^{0.002}_{0.002}$	23.27	0.69	0.50	9.46	$1.20^{0.18}_{0.17}$
28706	SF	$1.484^{0.105}_{0.012}$	23.38	0.72	0.25	9.45	$4.57^{5.21}_{3.61}$
33427	SF	$1.726^{0.001}_{0.003}$	23.90	0.44	0.23	9.26	$6.81^{13.82}_{10.25}$
36977	SF	$1.291^{0.001}_{0.002}$	23.41	0.65	0.31	9.25	$0.72^{0.15}_{0.14}$
32732	SF	$1.695^{0.001}_{0.007}$	23.58	0.43	0.60	9.24	$1.84^{0.51}_{0.44}$
28114	SF	$1.479^{0.005}_{0.003}$	24.32	0.45	0.11	9.05	$1.28^{1.25}_{0.68}$

Note. — Redshift uncertainties are 68% intervals derived by bootstrapping over the joint-fit G102+G141+photometry redshift probability distributions.